

# Water Resources Research

## RESEARCH ARTICLE

10.1029/2017WR021357

### Special Section:

Hydrology Delivers Earth System Sciences to Society (HESSS4): Improving and Integrating Knowledge Across Disciplines on Global Energy, Water and Carbon Cycles

### Key Points:

- Thermal remote sensing of evapotranspiration is critical due to uncertainties in aerodynamic temperature and conductance estimation
- We integrated radiometric temperature into Penman-Monteith Shuttleworth-Wallace framework to directly estimate conductances and evapotranspiration
- Moderate to low systematic errors in evapotranspiration across an aridity gradient in Australia

### Supporting Information:

- Supporting Information S1

### Correspondence to:

K. Mallick,  
kaniska.mallick@gmail.com;  
E. Toivonen,  
erika.a.toivonen@gmail.com

### Citation:

Mallick, K., Toivonen, E., Trebs, I., Boegh, E., Cleverly, J., Eamus, D., et al. (2018). Bridging thermal infrared sensing and physically-based evapotranspiration modeling: From theoretical implementation to validation across an aridity gradient in Australian ecosystems. *Water Resources Research*, 54, 3409–3435. <https://doi.org/10.1029/2017WR021357>.

Received 21 JUN 2017

Accepted 9 APR 2018

Accepted article online 16 APR 2018

Published online 13 MAY 2018

© 2018. The Authors.

This is an open access article under the terms of the Creative Commons Attribution-NonCommercial-NoDerivs License, which permits use and distribution in any medium, provided the original work is properly cited, the use is non-commercial and no modifications or adaptations are made.

## Bridging Thermal Infrared Sensing and Physically-Based Evapotranspiration Modeling: From Theoretical Implementation to Validation Across an Aridity Gradient in Australian Ecosystems

Kaniska Mallick<sup>1</sup> , Erika Toivonen<sup>1,2,3,4</sup> , Ivonne Trebs<sup>1</sup>, Eva Boegh<sup>5,6</sup>, James Cleverly<sup>7</sup> , Derek Eamus<sup>7</sup> , Harri Koivusalto<sup>2</sup>, Darren Drewry<sup>8,9</sup>, Stefan K. Arndt<sup>10</sup>, Anne Griebel<sup>10</sup>, Jason Beringer<sup>11</sup> , and Monica Garcia<sup>12,13</sup>

<sup>1</sup>Department of Environmental Research and Innovation, Luxembourg Institute of Science and Technology, Belvaux, Luxembourg, <sup>2</sup>Department of Built Environment, Aalto University School of Engineering, Espoo, Finland, <sup>3</sup>Climate System Research, Finnish Meteorological Institute, Helsinki, Finland, <sup>4</sup>Department of Physics, University of Helsinki, Helsinki, Finland, <sup>5</sup>Department of Science and Environment, Roskilde University, Roskilde, Denmark, <sup>6</sup>Now at Danish Agency for Data Supply and Efficiency, Copenhagen, Denmark, <sup>7</sup>Terrestrial Ecohydrology Research Group, School of Life Sciences, University of Technology Sydney, Broadway, NSW, Australia, <sup>8</sup>Jet Propulsion Laboratory, California Institute of Technology, Pasadena, CA, USA, <sup>9</sup>Joint Institute for Regional Earth System Science and Engineering, University of California, Los Angeles, CA, USA, <sup>10</sup>School of Ecosystem and Forest Sciences, University of Melbourne, Melbourne, Vic, Australia, <sup>11</sup>School of Agriculture and Environment, University of Western Australia, Crawley, WA, Australia, <sup>12</sup>Department of Environmental Engineering, Technical University of Denmark, Kgs. Lyngby, Denmark, <sup>13</sup>International Research Institute for Climate and Society, Earth Institute, Columbia University, Palisades, NY, USA

**Abstract** Thermal infrared sensing of evapotranspiration ( $E$ ) through surface energy balance (SEB) models is challenging due to uncertainties in determining the aerodynamic conductance ( $g_A$ ) and due to inequalities between radiometric ( $T_R$ ) and aerodynamic temperatures ( $T_0$ ). We evaluated a novel analytical model, the Surface Temperature Initiated Closure (STIC1.2), that physically integrates  $T_R$  observations into a combined Penman-Monteith Shuttleworth-Wallace (PM-SW) framework for directly estimating  $E$ , and overcoming the uncertainties associated with  $T_0$  and  $g_A$  determination. An evaluation of STIC1.2 against high temporal frequency SEB flux measurements across an aridity gradient in Australia revealed a systematic error of 10–52% in  $E$  from mesic to arid ecosystem, and low systematic error in sensible heat fluxes ( $H$ ) (12–25%) in all ecosystems. Uncertainty in  $T_R$  versus moisture availability relationship, stationarity assumption in surface emissivity, and SEB closure corrections in  $E$  were predominantly responsible for systematic  $E$  errors in arid and semi-arid ecosystems. A discrete correlation ( $r$ ) of the model errors with observed soil moisture variance ( $r = 0.33–0.43$ ), evaporative index ( $r = 0.77–0.90$ ), and climatological dryness ( $r = 0.60–0.77$ ) explained a strong association between ecohydrological extremes and  $T_R$  in determining the error structure of STIC1.2 predicted fluxes. Being independent of any leaf-scale biophysical parameterization, the model might be an important value addition in working group (WG2) of the Australian Energy and Water Exchange (OzEWEX) research initiative which focuses on observations to evaluate and compare biophysical models of energy and water cycle components.

**Plain Language Summary** Evapotranspiration modeling and mapping in arid and semi-arid ecosystems are uncertain due to empirical approximation of surface and atmospheric conductances. Here we demonstrate the performance of a fully analytical model which is independent of any leaf-scale empirical parameterization of the conductances and can be potentially used for continental scale mapping of ecosystem water use as well as water stress using thermal remote sensing satellite data.

### 1. Introduction

The determination of the aerodynamic temperature ( $T_0$ ) and conductance ( $g_A$ ) contributes to the principal uncertainty in regional-scale evapotranspiration ( $E$ ) mapping when using models based on thermal infrared

sensing (Kustas et al., 2016; Paul et al., 2014, 2013). To reduce this uncertainty, there is either a sincere need to accommodate and settle on a unified land surface parameterization for estimating  $T_0$  and  $g_A$ , or use analytical models independent of any empirical parameterization of these variables.

Land surface temperature or radiometric surface temperature ( $T_R$ ) obtained through thermal infrared remote sensing governs the land surface energy budget (Anderson et al., 2012; Kustas & Anderson, 2009), and thermal  $E$  models principally focus on surface energy balance (SEB) approach in which  $T_R$  represents the lower boundary condition to constrain the energy-water fluxes (Anderson et al., 2008; Mallick et al., 2014a, 2015; Norman et al., 1995). It satisfies the SEB equation (equations (1)–(3)) by altering  $T_0$  as well as by imposing constraints arising due to water stress on the biophysical conductances ( $g_A$  and  $g_C$ ) (a list of variables and symbols along with their units are given in Table A1).

$$R_N = H + \lambda E + G \quad (1)$$

$$(R_{S\downarrow} - R_{S\uparrow}) + (R_{L\downarrow} - \varrho \varepsilon T_R^4) = \rho c_p g_A (T_0 - T_A) + \frac{\rho c_p g_A g_C}{\gamma(g_A + g_C)} (e_0^* - e_A) + G \quad (2)$$

$$T_R = \left[ \frac{(R_{S\downarrow} - R_{S\uparrow}) + R_{L\downarrow} - \rho c_p g_A (T_0 - T_A) - \frac{\rho c_p g_A g_C}{\gamma(g_A + g_C)} (e_0^* - e_A) - G}{\varrho \varepsilon} \right]^{\frac{1}{4}} \quad (3)$$

State-of-the-art SEB models are based on estimating  $g_A$  and sensible heat flux ( $H$ ) while solving  $E$  (or latent heat flux,  $\lambda E$ ) as a residual SEB component (given  $R_N$  and  $G$  are known). However, the most serious assumption in estimating  $H$  concerns the use of  $T_R$  as a surrogate of  $T_0$  (Chávez et al., 2010; Colaizzi et al., 2004). Major drawbacks in the explicit use of  $T_R$  in SEB modeling are (a) the inequality between  $T_0$  and  $T_R$  ( $T_0 \neq T_R$ ) (Boulet et al., 2015; Chávez et al., 2010), (b) the unavailability of a universally agreed model to estimate  $T_0$ , which controls the transfer of sensible heat (Colaizzi et al., 2004), (c) nonunique relationship between  $T_0$  and  $T_R$  due to differences between the effective source-sink height of momentum and heat within vegetation substrate complex (Chávez et al., 2010; Holwerda et al., 2012; Troufleau et al., 1997), (d) the lack of a preeminent physically-based  $g_A$  model (Holwerda et al., 2012), and (e) bypassing the role of  $T_R$  on  $g_C$  in  $\lambda E$  modeling.

Despite the aforementioned shortcomings, emphasis on estimating  $H$  is motivated by the broad acceptance of the Monin-Obukhov Similarity Theory (MOST) or Richardson Number ( $R_i$ ) criteria for estimating  $g_A$ , and the requirement of minimum inputs for solving both  $g_A$  and  $H$ . However, estimating  $g_A$  using MOST or  $R_i$  approaches created further problems, particularly in relation to accommodating the inequalities between  $T_0$  and  $T_R$ , as well as in adapting the differences between  $g_A$  and the momentum conductance ( $g_M$ ) arising due to the differences in the roughness length of heat and momentum ( $z_{0H}$  and  $z_{0M}$ ) (Paul et al., 2014). The effects due to inequality between  $T_0$  and  $T_R$  were partially overcome by the inclusion of an “extra conductance” and the  $kB^{-1}$  term as a fitting parameter that adjusts the difference between  $z_{0H}$  and  $z_{0M}$  (Boegh et al., 2002; Su, 2002; Troufleau et al., 1997), and later through the inception of two-source soil-canopy modeling schemes (Anderson et al., 2007; Boulet et al., 2015; Colaizzi et al., 2012; Norman et al., 1995). However, SEB-based predictions of  $H$  (and  $\lambda E$ ) are conditional to empirical response functions of  $g_A$  (Ershadi et al., 2015; Kustas et al., 2016; Liu et al., 2007; Morillas et al., 2013; Paul et al., 2014; Timmermans et al., 2013) that have an uncertain transferability in space and time (Holwerda et al., 2012; van Dijk et al., 2015). In contemporary SEB modeling,  $g_A$  submodels are stand-alone, and lack the necessary physical feedback it should provide to  $g_C$ ,  $T_0$ , and vapor pressure deficit surrounding the evaporating surface ( $D_0$ ) (Cleverly et al., 2013). The feedback of  $g_A$  on  $g_C$  is critical in arid and semi-arid ecosystems where reduced soil moisture availability in conjunction with very high evaporative potential causes significant water stress in the soil-vegetation-atmosphere system, thereby resulting discrepancy between  $T_R$  and  $T_0$ . Thermal-based  $\lambda E$  modeling needs explicit consideration of such important biophysical feedbacks to reduce the existing uncertainties in arid and semi-arid ecosystems (Kustas et al., 2016).

The Penman-Monteith (PM) and Shuttleworth-Wallace (SW) models are mutually related and two of the most preeminent physical models for quantifying surface-to-air  $\lambda E$ . They are fundamentally constrained to account for the necessary feedbacks between  $\lambda E$ ,  $T_R$ ,  $D_0$ ,  $g_A$ , and  $g_C$  (Monteith, 1965; Shuttleworth & Wallace, 1985). The elemental connectivity of PM-SW with  $T_R$  originates from the first-order dependence of  $g_C$  and  $g_A$  on  $T_R$  (through soil moisture and  $T_0$ ). Despite their theoretical integrity, the integration of  $T_R$  into the PM-

SW model was not yet well established. Although the perception of combining the PM model with  $T_R$  was initiated by Jackson et al. (1981) in the Crop Water Stress Index (CWSI) formulation, it had later been acknowledged that using the PM method could produce large errors in  $\lambda E$  due to the underlying uncertainties in conductance estimates, particularly in sparsely vegetated and water-stressed ecosystems (Leuning et al., 2008; Morillas et al., 2013), such as the majority of ecosystems in Australia (Beringer et al., 2016).

Invigorated by the potential of thermal infrared data, Mallick et al. (2014a, 2015) proposed an integration of  $T_R$  into the PM model to directly estimate the conductances,  $\lambda E$ , and  $H$ , and to simultaneously overcome the empirical uncertainties in estimating  $g_A$  and  $T_0$ . The Surface Temperature Initiated Closure (STIC) (Mallick et al., 2014a, 2015) is a unique framework based on analytical solutions for  $g_A$ ,  $g_C$ , and  $T_0$ . Initial studies with different versions of STIC primarily focused on validation of  $H$ ,  $\lambda E$ , and its partitioning, using moderate (coarse) spatial (temporal) resolution remote sensing data (STIC1.0; Mallick et al., 2014a), and understanding the impacts of thermal versus humidity based water stress constraints on  $\lambda E$  (STIC1.1; Mallick et al., 2015). However, the early versions of STIC could only partially bridge  $T_R$  and SEB modeling due to structural inadequacies for establishing surface versus aerodynamic feedbacks (Mallick et al., 2015). A later version of STIC (STIC1.2) (Mallick et al., 2016) integrates  $T_R$  into the PM-SW system to establish the required feedback between  $T_R$  and  $\lambda E$ , along with aerodynamic temperature, humidity, and conductances. In a recent study, STIC1.2 was applied for evaluation of biophysical conductances and assessing their controls on evapotranspiration partitioning in the Amazon basin (Mallick et al., 2016). However, evaluating the performance of STIC1.2 across an aridity gradient with data of high temporal resolution is on one hand essential to understand the role of  $T_R$  in STIC1.2 in hydrologically extreme natural ecosystems, and on the other to evaluate the limitations of this analytical SEB model before extending its future applicability for regional-scale  $E$  mapping.

The combination of prevailing arid/semi-arid ecosystems, ecohydrological heterogeneity, and the availability of continuous SEB flux observations make Australia an excellent test bed. Present study reports an in-depth evaluation of STIC1.2 by exploring eddy covariance (EC) observations from a range of diverse ecosystems of the OzFlux network (Beringer et al., 2016) across a large aridity gradient in Australia as a way forward to reduce  $T_0$  and  $g_A$  uncertainties in regional-scale  $E$  mapping as well as to efficiently bridge  $T_R$  and SEB modeling. Our study addressed the following research questions:

1. What is the performance of STIC1.2 when evaluated with high temporal resolution data across an aridity gradient in Australia?
2. How do  $T_R$  and environmental variables affect the performance of STIC1.2 across ecohydrological extremes from arid to mesic ecosystems?
3. Is there an association between ecohydrological conditions and  $T_R$  in determining the errors and variability of water and energy flux components predicted by STIC1.2?

The novelties of the present study are: (a) an extensive evaluation of STIC1.2 from dry to wet ecohydrological extremes at multiple temporal scales (from half-hourly to annual), (b) intercomparison with previous versions of STIC, (c) analyzing the sensitivity of  $\lambda E$  and conductances to  $T_R$ , as well as application of multivariate statistics (e.g., principal component analysis) to understand the impacts of  $T_R$  and environmental variables on the error characteristics of STIC1.2 derived  $\lambda E$  from arid to mesic climate, and (d) identification of the integrated role of ecohydrological conditions and  $T_R$  on errors and variability of SEB flux predictions by STIC1.2.

## 2. Why Australia?

Australia is a predominantly dry continent with substantial fluctuations in precipitation and primary production (Cleverly et al., 2016). Limited water resources, drought vulnerability, high evaporative demand, and growing water requirements are continuously increasing pressure on sustainable management of water resources. The Millennium Drought from 2001 to 2009 dramatically ended with a “big wet” in 2010–2012 coinciding with the largest La Niña in over 70 years (Cleverly et al., 2016; van Dijk et al., 2013). A major part of the Australian continent is arid (38%) or semi-arid (36%) (Beringer et al., 2016) with canopy cover of less than 50% across most of the continent (Glenn et al., 2011). In contrast, there are locations where annual average precipitation exceeds 4,000 mm (Glenn et al., 2011). In most areas of the continent, potential evaporation ( $E_p$ ) exceeds precipitation ( $P$ ), and approximately 90% of  $P$  returns back to the atmosphere as  $E$ .

(Glenn et al., 2011) with the residue generating surface and groundwater resources (Guerschman et al., 2009). Strong land-atmosphere coupling in these regions makes the estimation of SEB fluxes very sensitive to the boundary conditions and underlying assumptions of biophysical parameterization, a situation that is often confounded by extreme heterogeneity in evaporation versus transpiration and their contrasting responses to surface soil water content. Hence, observation, monitoring, and prediction of water and energy flux components are imperative in these regions to meet the challenge of developing and implementing sustainable water resource management decisions (Martens et al., 2016). Therefore, detailed evaluation of a physically-based SEB model like STIC1.2 is the prerequisite before applying it for a reliable prediction and management of water resources in Australia and globally.

### 3. Methodology

#### 3.1. Theory

STIC (version STIC1.2) is a one-dimensional SEB model that treats soil-vegetation as a single unit (Figure 1). The fundamental assumption in STIC is the first-order dependence of  $g_A$  and  $g_C$  on aerodynamic temperature ( $T_0$ ) and soil moisture ( $\theta$ ) through  $T_R$ , which allows direct integration of  $T_R$  into the PM-SW system (Mallick et al., 2016). The integration of  $T_R$  into PM-SW system is done by first estimating aggregated surface moisture availability ( $M$ ) as a function of  $T_R$ , followed by simultaneously constraining the two biophysical conductances through  $M$  in an analytical framework. STIC1.2 exploits radiation (net radiation ( $R_N$ ), ground heat flux ( $G$ )) and meteorological variables (air temperature ( $T_A$ ), relative humidity ( $R_H$ ) or vapor pressure ( $e_A$ ) at the reference level) in conjunction with  $T_R$  observations as external inputs.

The expressions of  $\lambda E$  and  $H$  according to the PM equation are as follows (Monteith, 1965):

$$\lambda E = \frac{s\phi + \rho c_P g_A D_A}{s + \gamma \left(1 + \frac{g_A}{g_C}\right)} \quad (4a)$$

$$H = \frac{\gamma \phi \left(1 + \frac{g_A}{g_C}\right) - \rho c_P g_A D_A}{s + \gamma \left(1 + \frac{g_A}{g_C}\right)} \quad (4b)$$

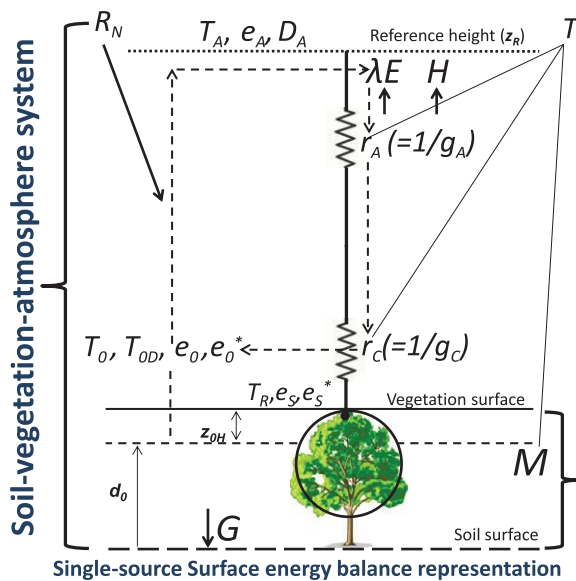


**Figure 1.** Schematic representation of one-dimensional description of STIC1.2. In STIC1.2, a feedback is established between the surface layer evaporative fluxes and source/sink height mixing and coupling, and the connection is shown in dotted arrows between  $e_0$ ,  $e_0^*$ ,  $g_A$ ,  $g_C$ , and  $\lambda E$ . Here  $r_A$  and  $r_C$  are the aerodynamic and canopy (or canopy-substrate complex in case of partial vegetation cover) resistances,  $g_A$  and  $g_C$  are the aerodynamic and canopy conductances (reciprocal of resistances),  $e_S^*$  is the saturation vapor pressure at the surface,  $e_0^*$  is the saturation vapor pressure at the source/sink height,  $T_0$  is the source/sink height temperature (i.e., aerodynamic temperature) that is responsible for transferring the sensible heat ( $H$ ),  $e_0$  is the source/sink height vapor pressure,  $e_S$  is the vapor pressure at the surface,  $z_{0H}$  is the roughness length for heat transfer,  $d_0$  is the displacement height,  $T_R$  is the radiometric surface temperature,  $T_{0D}$  is the source/sink height dewpoint temperature,  $M$  is the surface moisture availability or evaporation coefficient,  $R_N$  and  $G$  are net radiation and ground heat flux,  $T_A$ ,  $e_A$ , and  $D_A$  are temperature, vapor pressure, and vapor pressure deficit at the reference height ( $z_R$ ),  $\lambda E$  is the latent heat flux, respectively.

For a full vegetation and (or) bare surface,  $g_C$  represents the canopy conductance and (or) bare surface conductance, respectively. In the case of partial canopy cover,  $g_C$  represents an aggregated surface conductance of both canopy and soil. The effects of this simplified representation of aggregated  $g_C$  on the performance of STIC1.2 is represented in Figures 9b, 9d, and 9f which shows the residual  $\lambda E$  error (modeled minus observed  $\lambda E$ ) versus  $g_C$  for different vegetation types.

The two unknown “state variables” in equations (4a) and (4b) are  $g_A$  and  $g_C$ , and the main goal of STIC1.2 is to find an analytical solution of the two unobserved conductances from measurements of radiative, meteorological, and radiometric conditions (Mallick et al., 2014a, 2015, 2016). This will simultaneously find a “closure” of the PM model. As neither  $g_A$  nor  $g_C$  can be measured at the canopy-scale or at large spatial scales (van Dijk et al., 2015), a “closure” of the PM equation is only possible through an analytical estimation of the conductances. Consequently, multiple “state equations” were formulated to obtain closed-form expressions of  $g_A$  and  $g_C$ . In the state equations, a direct connection of  $T_R$  (through  $M$ ) is initiated in the expression of evaporative fraction ( $\Lambda$ ), which is simultaneously propagated into equations of  $g_A$ ,  $g_C$ , and  $T_0$  (equations (5)–(8)).

$$\Lambda = \frac{2\alpha s}{2s + 2\gamma + \gamma \frac{g_A}{g_C} (1+M)} \quad (5)$$

$$T_0 = T_A + \left( \frac{e_0 - e_A}{\gamma} \right) \left( \frac{1 - \Lambda}{\Lambda} \right) \quad (6)$$

$$g_A = \frac{\phi}{\rho c_P \left[ (T_0 - T_A) + \left( \frac{e_0 - e_A}{\gamma} \right) \right]} \quad (7)$$

$$g_C = g_A \frac{(e_0 - e_A)}{(e_0^* - e_0)} \quad (8)$$

The functional forms of equations (5)–(8) and their detailed derivations are given in the supporting information and in Mallick et al. (2014a, 2015, 2016). Given values of  $M$ ,  $R_N$ ,  $G$ ,  $T_A$ , and  $R_H$  or  $e_A$ , the four state equations (equations (5)–(8)) can be solved simultaneously to derive analytical solutions for the four unobserved state variables. However, the analytical solutions to the four state equations have three accompanying unknowns;  $e_0$  (vapor pressure at the source/sink height),  $e_0^*$  (saturation vapor pressure at the source/sink height), and Priestley-Taylor coefficient ( $\alpha$ ) (Priestley & Taylor, 1972), and as a result there are four equations with seven unknowns. Consequently, an iterative solution must be found to determine the three unknown variables (as described in supporting information) (also in Mallick et al., 2016). For estimating source/sink height vapor pressures we applied equation (8) from Shuttleworth and Wallace (1985), and thus STIC1.2 uniquely combines both the Penman-Monteith and Shuttleworth-Wallace (PM-SW) models (described in supporting information) (also Mallick et al., 2016). In equation (8), the Priestley-Taylor coefficient ( $\alpha$ ) appeared due to using the Advection-Aridity (AA) hypothesis (Brutsaert & Stricker, 1979) for deriving the state equation of  $\Lambda$  (Mallick et al., 2016, 2015) (details in supporting information). However, instead of optimizing  $\alpha$  as a “fixed parameter,”  $\alpha$  is dynamically estimated by constraining it as a function of  $M$ , conductances, aerodynamic vapor pressure, and temperature (Mallick et al., 2016). The derivation of the equation for  $\alpha$  is described in supporting information.

STIC1.2 consists of a feedback loop describing the relationship between  $T_R$  and  $\lambda E$ , coupled with canopy-atmosphere components relating  $\lambda E$  to  $T_0$  and  $e_0$  (Mallick et al., 2016). For estimating  $M$ ,  $T_R$  is extensively used in a physical retrieval framework (detailed in SI) (also in Mallick et al., 2016), which allows an integration of  $T_R$  into a physically-based SEB model. Upon finding analytical solution of  $g_A$  and  $g_C$ , both the variables are returned into equations (4a) and (4b) to directly estimate  $\lambda E$  and  $H$ .

### 3.2. Estimation of $T_R$

Estimation of  $T_R$  was based on the observed upwelling longwave radiation ( $R_{L\uparrow}$ ) and the Stefan-Boltzmann equation  $\left[ T_R = \left( \frac{R_{L\uparrow}}{\delta \epsilon} \right)^{0.25} \right]$  (Formetta et al., 2016; Park et al., 2008; Sun & Pinker, 2003) ( $\epsilon$  is the infrared surface emissivity,  $\delta$  is the Stefan-Boltzmann constant). Upwelling longwave radiation was directly measured with pyrgeometer in all the study sites. The Advanced Spaceborne Thermal Emission and Reflection Radiometer (ASTER) Global Emissivity Dataset (GED) land surface emissivity data product (Göttsche & Hulley, 2012; Hulley et al., 2015) (product name: AG100V003; spatial resolution: 100 m, temporal frequency: static) ([https://lpdaac.usgs.gov/dataset\\_discovery/community/community\\_products\\_table](https://lpdaac.usgs.gov/dataset_discovery/community/community_products_table)) was used in the inverted Stefan-Boltzmann equation for estimating  $T_R$ . This  $\epsilon$  database is developed by the National Aeronautics and Space Administration’s (NASA) Jet Propulsion Laboratory (JPL), California Institute of Technology, and ASTER data from 2000 to 2008 are used to generate this infrared emissivity record. For every site, the corresponding  $\epsilon$  is given in Table 1.

### 3.3. SEB Closure

The statistical intercomparisons of STIC1.2 results against SEB flux observations were performed by forcing energy balance closure by adding energy to  $\lambda E$  and  $H$  in proportion to the measured Bowen ratio ( $H/\lambda E$ ; BREB-closure) (Bowen, 1926) as described by Chávez et al. (2005) and later adopted by Anderson et al. (2008) and Mallick et al. (2014a, 2015, 2016). However, in order to understand the effects of SEB closure correction methods on the statistical error metric, residual SEB closure correction (RES-closure) was also tested in which actual  $\lambda E$  observations were neglected (Majozi et al., 2017), and  $\lambda E$  was estimated as a residual of

**Table 1**  
An Overview of Sites, Their Aridity Index (AI) Class and Characteristics (Numbers in the Parentheses Represent the Coefficient of Variation)

Aridity index (AI) class	Site name	OzFlux ID	Region	Latitude (S) Longitude (E)	World ecoregion	Land cover	AI	Annual $T_A$ (°C)	Annual P (mm yr <sup>-1</sup> )	Annual E (mm yr <sup>-1</sup> )	E/R <sub>N</sub>	$\varepsilon$ %	EBC %	Data availability $\lambda E \& H$ (%)
Arid (0 < AI < 0.2)	Alice Springs	AU-ASM	Northern Territory	-22.28° 133.25°	Deserts and Xeric shrublands	Semi-arid mulga (Acacia aneura) ecosystem	0.04–0.11	(−4) to 46	306 (58)	141 (100)	0.800	60–61	95	
	Calperum	AU-Epr	South Australia	-34.00° 140.59°	Mediterranean woodlands	Recovering mallee woodland	0.05–0.06	12–45	240 (60)	257 (77)	0.13	0.800	72–78	
Great Western Woodlands	AU-GWW	Western Australia	-30.19° 120.65°	Mediterranean woodlands	Temperate woodland, Shrubland and mallee	0.05–0.14	5–33	240 (41)	135 (77)	0.17	0.810	56–58		
Ti Tree East	AU-TTE	Northern Territory	-22.29° 133.64°	Deserts and Xeric shrublands	Grassy mulga woodland and Cynobia/ Triodia savanna	0.05–0.11	(−4) to 46	305 (80)	144 (100)	0.11	0.835	72–75		
Semi-arid (0.2 < AI < 0.5)	Gingin	AU-Gin	Western Australia	-31.38° 115.71°	Mediterranean woodlands	Coastal heath Banksia woodland	0.20–0.26	19–30	641 (19)	486 (63)	0.29	0.805	77–78	
	Jaxa (Yanco)	AU-Ync	New South Wales	-34.99° 146.29°	Temperate grassland	Grassland	0.30–0.41	12–37	465 (34)	207 (100)	0.10	0.800	57–76	
Riggs Creek	AU-Rig	Victoria	-36.65° 145.58°	Pasture	Dryland agriculture	0.45–0.46	12–26	650 (23)	297 (84)	0.30	0.910	80–81		
Sturt Plains	AU-Spt	Northern Territory	-17.15° 133.35°	Tropical grassland	Low lying plain dominated by Mitchell Grass	0.22–0.33	11–39	640 (37)	454 (100)	0.28	0.880	82–93		
Whroo	AU-Whr	Victoria	-36.67° 145.03°	Temperate woodlands	Boxwoodland	0.20–0.22	3–30	558 (52)	443 (62)	0.27	0.810	93–95		
Wombat	AU-Wom	Victoria	-37.42° 144.09°	Temperate broadleaf forest	Dry sclerophyll eucalypt forest	0.23–0.39	1–30	650 (10)	653 (62)	0.43	0.925	71–73		
Mesic (0.5 < AI)	Cowbay	AU-Cow	Queensland	-16.24° 144.09°	Tropical and subtropical moist broadleaf forests	Complex mesophyll vine forest	2.30–2.90	11–39	4,000 (10)	745 (55)	0.61	0.955	89–91	
	Cumberland Plains	AU-Cum	New South Wales	-33.62° 150.72°	Temperate woodlands	Dry sclerophyll	0.56–0.76	3–29	800 (24)	486 (66)	0.43	0.885	81–91	
Dry River	AU-Dry	Northern Territory	-15.26° 132.37°	Tropical savannas	Open forest savanna	0.50–0.73	14–37	895 (36)	679 (73)	0.47	0.970	80–81		
Howard Springs	AU-How	Northern Territory	-12.49° 131.15°	Tropical savannas	Tropical savanna (wet)	0.53–0.64	20–33	1,700 (25)	1,190 (60)	0.56	0.870	85–91		
Tumbarumba	AU-Tum	New South Wales	-35.66° 148.15°	Temperate broadleaf and mixed forest	Wet temperate sclerophyll eucalypt	0.65–0.77	(−10) to 30	1,000 (15)	955 (90)	0.68	0.970	72–75		

$R_N$ ,  $G$ , and  $H$ . Caution in using RES-closure method has been previously given by Barr et al. (2012) because it is very unlikely that measurements of  $R_N$ ,  $G$  or  $H$  are without error.

## 4. Data Sets and Statistical Analysis

### 4.1. Eddy Covariance and Meteorological Quantities

In the present analysis, we have used data from the regional Australian and New Zealand EC flux tower network, OzFlux (<http://data.ozflux.org.au/portal/pub/listPubCollections.jspx>). OzFlux EC stations are distributed among ecohydrologically contrasting landscapes in Australia and New Zealand to provide national data of energy, water, and carbon fluxes at a continental scale to improve our understanding of the responses of these surface-atmosphere fluxes of Australian ecosystems to current climate as well as future climate change (Beringer et al., 2016).

We explored the level-3 quality controlled and harmonized surface flux and meteorological data for the years 2013 and 2014 from 15 (out of 26) active Australian OzFlux sites located across nine different ecoregions in Australia (Figure 2 and Table 1): deserts and xeric shrublands (AU-ASM, AU-TTE), pasture (AU-Rig), Mediterranean woodlands (AU-Cpr, AU-Gin, AU-GWW), temperate broadleaf (and mixed) forest (AU-Tum, AU-Wom), temperate grassland (AU-Ync), temperate woodlands (AU-Cum, AU-Whr), tropical and subtropical moist broadleaf forest (AU-Cow), tropical grassland (AU-Stop), and tropical savannas (AU-How, AU-Dry). We divided these sites into three broad aridity classes based on their aridity index (AI) (ratio of annual  $P$  and  $E_P$ ; i.e.,  $P/E_P$ ): arid ( $0 < AI < 0.2$ , AU-ASM, AU-Cpr, AU-GWW, and AU-TTE); semi-arid ( $0.2 < AI < 0.5$ , AU-Gin, AU-Rig, AU-Stop, AU-Whr, AU-Wom, and AU-Ync); and mesic (subhumid and humid) ( $0.5 < AI$ , AU-Cow, AU-Cum, AU-Dry, AU-How, and AU-Tum) (<http://www.bom.gov.au>). In Table 1, annual values of  $P$  and  $T_A$  are the climatological averages of every site which are reported in <http://www.ozflux.org.au/monitoringsites/>. Annual  $E$  and  $R_N$  were computed from the available EC tower data sets for 2013 and 2014. Annual  $E_P$  was computed from FAO (Food and Agricultural Organisation) Penman-Monteith equation (Allen et al., 1998).

The main reason for selecting 2013 and 2014 was the rainfall deficit which followed the anomalously wet period of 2010 and 2011 in Australia (Cleverly et al., 2016; Ma et al., 2016) and continued to worsen to severe drought through 2014 across the continent (<http://www.bom.gov.au/climate/drought/archive/>). According to these criteria, data availability in these 2 years coincided for the selected 15 sites.

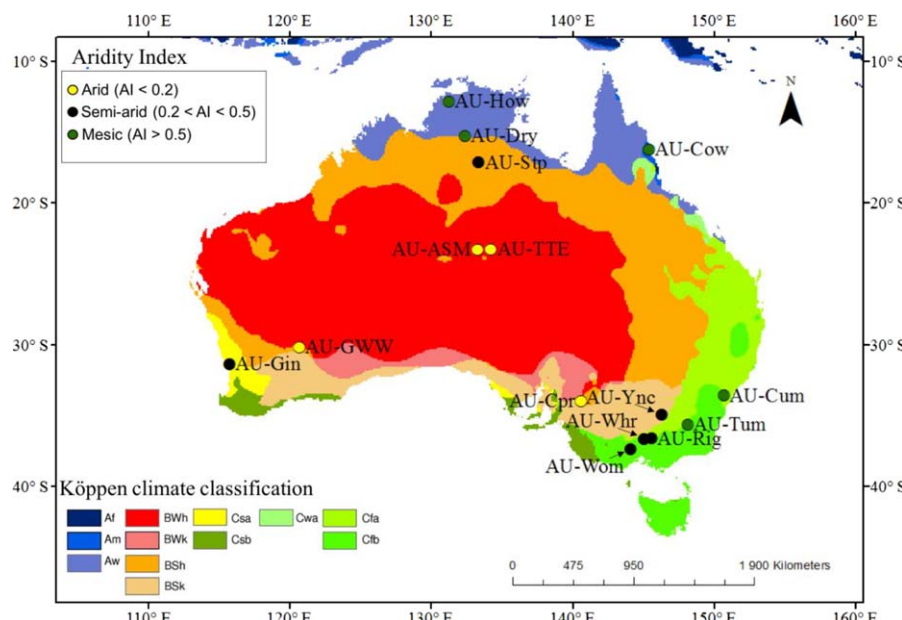


**Figure 2.** Climatic map of Australia with the distribution of 15 eddy covariance sites (source of the base map: <http://people.eng.unimelb.edu.au/mpeel/Koppen/Australia.jpg>).

The data are available at half-hourly temporal resolution, with an exception at AU-Tum where the temporal resolution of the data is 1 h. Data used for this analysis included time series of surface energy balance fluxes ( $R_N$ ,  $\lambda E$ ,  $H$ ,  $G$ ), shortwave and longwave radiation components ( $R_{S\downarrow}$ ,  $R_{S\uparrow}$ ,  $R_{L\downarrow}$ ,  $R_{L\uparrow}$ ), and hydrometeorological variables (e.g.,  $T_A$ ,  $R_H$ ,  $u$ ,  $u^*$ ,  $\theta$ , and  $P$ ). A general description of the site characteristics can be found in Table 1 and also in Beringer et al. (2016). Daily SEB fluxes (in  $\text{W m}^{-2}$ ) were computed by averaging half-hourly (hourly for AU-Tum) observed fluxes and those predicted by STIC1.2. Monthly and annual  $E$  (in mm) and  $H$  (converted to water equivalent in mm) (<http://www.fao.org/docrep/x0490e/x0490e07.htm>) were computed by summing daily  $\lambda E$  and  $H$  values. We did not perform any gap filling, which implies that missing observed or estimated subdaily or daily  $\lambda E$  and  $H$  values (for data availability see Table 1) were not included in the computation.

Performance of STIC 1.2 was also evaluated for dry and wet seasons (Appendix A2), whereby the seasons were defined based on monthly  $P$  and  $\theta$ . The timing and duration of the seasons varied between different sites. A table of dry and wet seasons for the individual sites are given in Table A3.

## 4.2. Statistical Analysis

### 4.2.1. Multitemporal SEB Flux Assessment

In order to evaluate the performance of STIC1.2, we used different statistical metrics: root-mean-square deviation (RMSD), relative root-mean-square deviation (RRMSD), the coefficient of determination ( $R^2$ ), mean absolute percentage deviation (MAPD), and the ratio of squared systematic RMSD to squared RMSD ( $\text{RMSDs}^2/\text{RMSD}^2$ ) (equations (A1)–(A4) in Appendix). Predicted  $\lambda E$  and  $H$  were compared with observed values for each study site at sub-daily, daily, and annual scales. Results and discussions on multitemporal SEB flux estimation statistics are given in sections 5.1 and 6.1, respectively.

### 4.2.2. Assessing the Role of $T_R$ and Associated Environmental Variables on the Performance of STIC1.2

A sensitivity analysis and a Principal Component Regression (PCR) analysis (Jolliffe, 2002) were performed to assess the impact of  $T_R$  and environmental variables on the relative change in  $\lambda E$  error (in percent) and residual error of  $\lambda E$  (i.e.,  $\Delta_{\lambda E}$  = difference between  $\lambda E$  predicted by STIC1.2 and observed  $\lambda E$ ). Sensitivity of  $\lambda E$  to  $T_R$  was tested by introducing random uncertainty in the surface emissivity to generate uncertain  $T_R$  scenarios at half-hourly time steps. The relative change in  $\lambda E$  error due to the relative change in  $T_R$  was estimated for every time step and correlation between them was evaluated for different classes of  $\theta$  and  $E_p/\phi$  ratios. PCR was performed on a correlation matrix of five variables which are:  $T_R$ ,  $D_A$ ,  $\phi$ , wind speed ( $u$ ), and  $\Delta_{\lambda E}$ . The correlation between  $\Delta_{\lambda E}$  and principal component (PC) is known as “loading.” Loadings close to  $\pm 1$  indicate that the variable has substantial impact on  $\Delta_{\lambda E}$ . PCs with high loadings generally explain maximum variances in  $\Delta_{\lambda E}$  and are considered in evaluating the impacts on  $\Delta_{\lambda E}$ . Results of the sensitivity analysis and PCR are presented in section 5.2 with extended discussions in section 6.2.

### 4.2.3. Relationship Between Ecohydrological Factors and $T_R$ in Determining the Errors and Variability of SEB Fluxes Predicted by STIC1.2

To examine the link between ecohydrological conditions and  $T_R$  on the SEB flux predictions, we further investigated the patterns of MAPD in daily  $\lambda E$  and  $H$  in comparison to the coefficient of variation of observed soil moisture ( $cV_\theta$ ), annual evaporative index (i.e., annual  $E/R_N$ ), climatic dryness (i.e., annual  $E_p/P$ ) (Donohue et al., 2010), and emissivity ( $\varepsilon$ ), which are considered to represent the ecohydrological characteristics of ecosystems that are intrinsically related to  $T_R$ . Arid and semi-arid ecosystems generally have large variations in  $\varepsilon$  (Hulley et al., 2010; Masiello et al., 2014) which is mostly associated with high  $cV_\theta$ , low  $E/R_N$ , and high  $E_p/P$  (high evaporative demand and low precipitation). Therefore, assessing the effects of a single value of  $\varepsilon$  on the predictive capacity of STIC1.2 is crucial. Results of the correlation analysis between MAPD of daily  $\lambda E$  (and  $H$ ) with  $\varepsilon$ , annual  $cV_\theta$ , annual  $E/R_N$ , and annual  $E_p/P$  of each site is presented in section 5.3 and discussions are elaborated in section 6.3.

## 5. Results

### 5.1. Performance of STIC1.2 Across an Aridity Gradient in Australia

The box-plots of statistical errors of half-hourly  $\lambda E$  for three ecohydrologically contrasting ecosystem classes revealed STIC1.2 to explain 60–85% of the observed  $\lambda E$  variability ( $R^2$  0.60–0.85), with mean MAPD of 30–50%, and mean RMSD 36–55  $\text{W m}^{-2}$  in the mesic and semi-arid sites (Figures 3a, 3c, and 3e, please see Table 2 for site statistics). For the arid sites, STIC1.2 explained 40% of the observed  $\lambda E$  variability, with RMSD

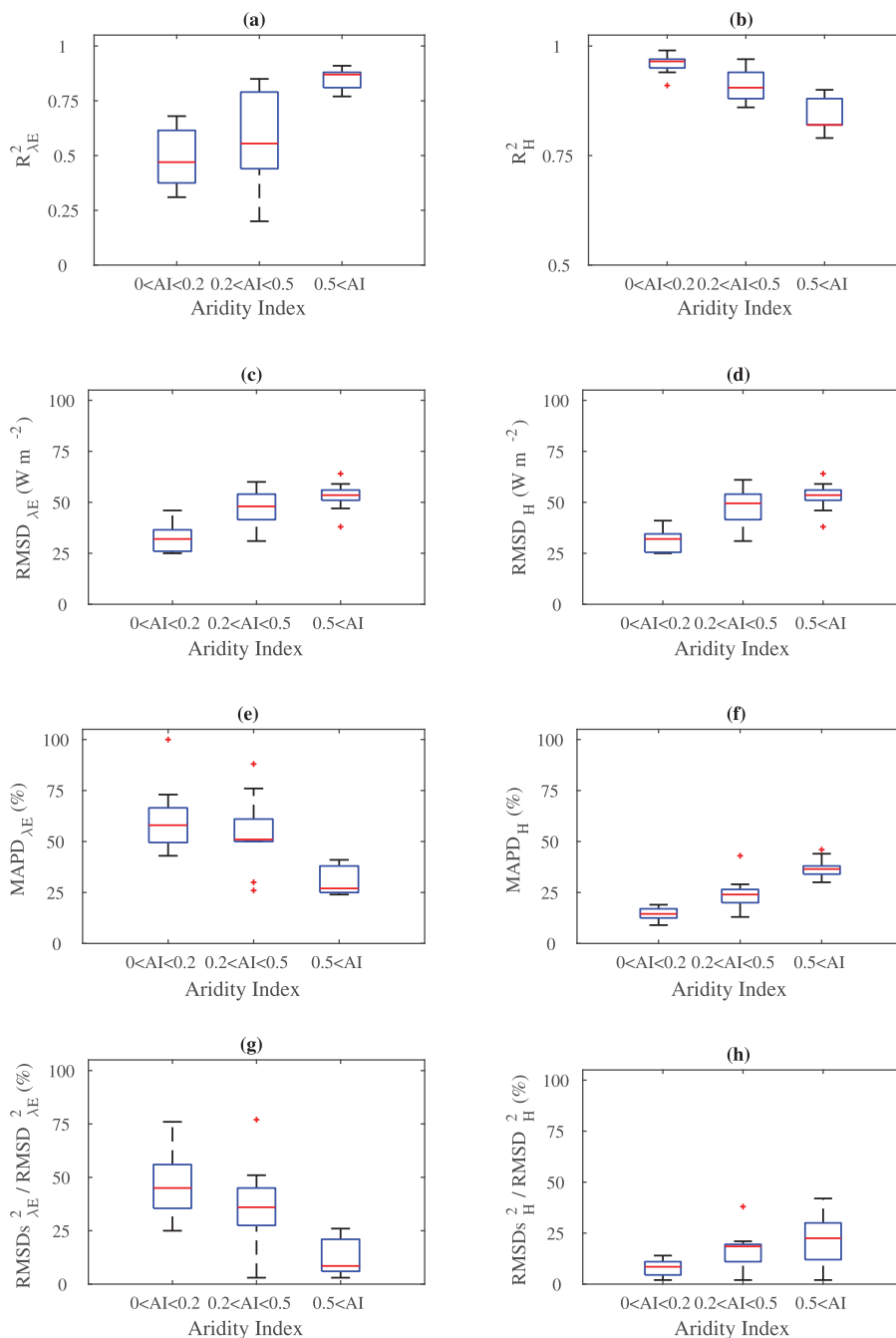


**Figure 3.** (a) Boxplots and whiskers of  $R^2$ , (b) MAPD, (c) RMSD, and (d)  $RMSD_s^2/RMSD_2$  between  $\lambda E$  and  $H$  predicted by STIC1.2 versus observations in OzFlux ecosystems of contrasting aridity. The lower and upper bound of the box and the red line inside represents the first and third quartiles, and median values. The lower and upper whiskers represent minimum and maximum values of the statistics and the red line in the boxplot represent the mean values of the statistical metrics.

of  $26\text{--}46 \text{ W m}^{-2}$  (average  $36 \text{ W m}^{-2}$ ) (78% of the observed mean) and relatively high MAPD (60%) (Figures 3a, 3c, and 3e). The average ratio of  $RMSD_s^2/RMSD^2$  (i.e., systematic RMSD, %) was moderate to low in Semi-arid (35%, range 24–48%) and mesic (10%, range 3–23%) ecosystems (Figure 3g), which increased to 45% (range 30–60%) in the arid ecosystems, thus revealing high systematic  $\lambda E$  error (along with high percent RMSD) in the water-limited ecosystems as compared to the radiation-limited ecosystems (Figure 3g). The predictive accuracy of  $H$  followed the opposite pattern compared to  $\lambda E$ , featuring maximum  $R^2$  (0.85–

**Table 2**

Error Statistics of Sub-daily  $\lambda E$  and  $H$  Derived With STIC1.2 on 15 EC Sites Covering Three Ecohydrologically Contrasting OzFlux Ecosystems of Different Aridity Classes as Defined in Table 1

Aridity class	Site name	Year	$\lambda E$			$H$		
			RMSD (W m <sup>-2</sup> )	R <sup>2</sup>	MAPD (%)	RMSD <sub>s</sub> <sup>2</sup> / RMSD <sup>2</sup> (%)	RMSD (W m <sup>-2</sup> )	R <sup>2</sup>
Arid (0 < AI < 0.2)	AU-ASM	2013	26	0.31	73	25	25	0.99
		2014	39	0.63	52	52	35	0.97
	AU-Cpr	2013	30	0.39	58	34	30	0.97
		2014	25	0.36	58	37	25	0.96
	AU-GWW	2013	34	0.54	47	60	34	0.94
		2014	34	0.60	43	42	34	0.96
	AU-TTE	2013	26	0.40	100	48	26	0.97
		2014	46	0.68	60	76	41	0.91
	AU-Gin	2013	53	0.55	50	34	53	0.90
		2014	54	0.54	54	24	54	0.91
Semi-arid (0.2 < AI < 0.5)	AU-Ync	2013	39	0.27	65	77	39	0.94
		2014	31	0.20	88	45	31	0.97
	AU-Rig	2013	60	0.48	57	51	61	0.86
		2014	59	0.40	76	45	60	0.87
	AU-Stp	2013	44	0.76	51	38	44	0.88
		2014	50	0.82	51	42	52	0.88
	AU-Whr	2013	43	0.56	51	21	43	0.94
		2014	46	0.58	50	32	47	0.94
	AU-Wom	2013	40	0.85	26	3	40	0.95
		2014	54	0.82	30	31	54	0.89
Mesic (0.5 < AI)	AU-Cow	2013	38	0.91	24	9	38	0.82
		2014	47	0.85	31	5	46	0.82
	AU-Cum	2013	51	0.81	41	25	51	0.89
		2014	52	0.77	40	8	52	0.90
	AU-Dry	2013	54	0.88	25	21	54	0.80
		2014	64	0.80	38	26	64	0.82
	AU-How	2013	55	0.89	24	7	55	0.82
		2014	59	0.87	26	16	59	0.79
	AU-Tum	2013	56	0.87	27	6	56	0.87
		2014	53	0.88	27	3	53	0.88

0.95) and minimum errors (10–25% MAPD and 35–50 W m<sup>-2</sup> RMSD) in the water-limited ecosystems as compared to the wet ecosystems with R<sup>2</sup> of 0.80, MAPD 37%, and RMSD 55 W m<sup>-2</sup>, respectively (Figures 3b, 3d, and 3f). Interestingly, the average ratio of RMSD<sub>s</sub><sup>2</sup>/RMSD<sup>2</sup> varied between 10% and 25% (Figure 3h), thus revealing low systematic errors in  $H$  estimates for a broad spectrum of ecohydrologically contrasting environments.

The statistical metrics of daily  $\lambda E$  and  $H$  was better than the half-hourly error statistics in the semi-arid and mesic ecosystems, with RMSD 11–18 W m<sup>-2</sup> (12–20 W m<sup>-2</sup> for  $H$ ), MAPD of 20–39% (24–37% for  $H$ ), R<sup>2</sup> of 0.65–0.84 (0.73–0.87 for  $H$ ), slope and offsets of regression to the order of 0.70–0.84 (0.67–0.79 for  $H$ ) and 9–10 W m<sup>-2</sup> (19–20 W m<sup>-2</sup> for  $H$ ), respectively (Figures 4c–4f). As for subdaily statistics, the predictive errors in daily  $H$  were lowest (12 W m<sup>-2</sup> RMSD and 12% MAPD) in the arid ecosystems, whereas percent  $\lambda E$  errors were highest (55% MAPD) (due to low mean  $\lambda E$ ) (Figures 4a and 4b). An evaluation of the annual SEB fluxes revealed a very good agreement between observed and predicted  $E$  and  $H$ , where STIC1.2 explained 97% of the measured variability, with MAPD and RMSD to the order of 10% and 55–84 mm, respectively (Figures 5a and 5b).

An intercomparison of STIC1.2 half-hourly error statistics with the two previous versions (STIC1.0 and STIC1.1) revealed maximum improvement in the performance of STIC1.2 for arid and semi-arid ecosystems (as compared to the mesic ecosystems) (Figure A1). Among the different model versions, notable differences in MAPD (20–60%, 8–40%, and 5–30%) and RMSD (25–50 W m<sup>-2</sup>, 20–40 W m<sup>-2</sup>, and 18–60 W m<sup>-2</sup>)

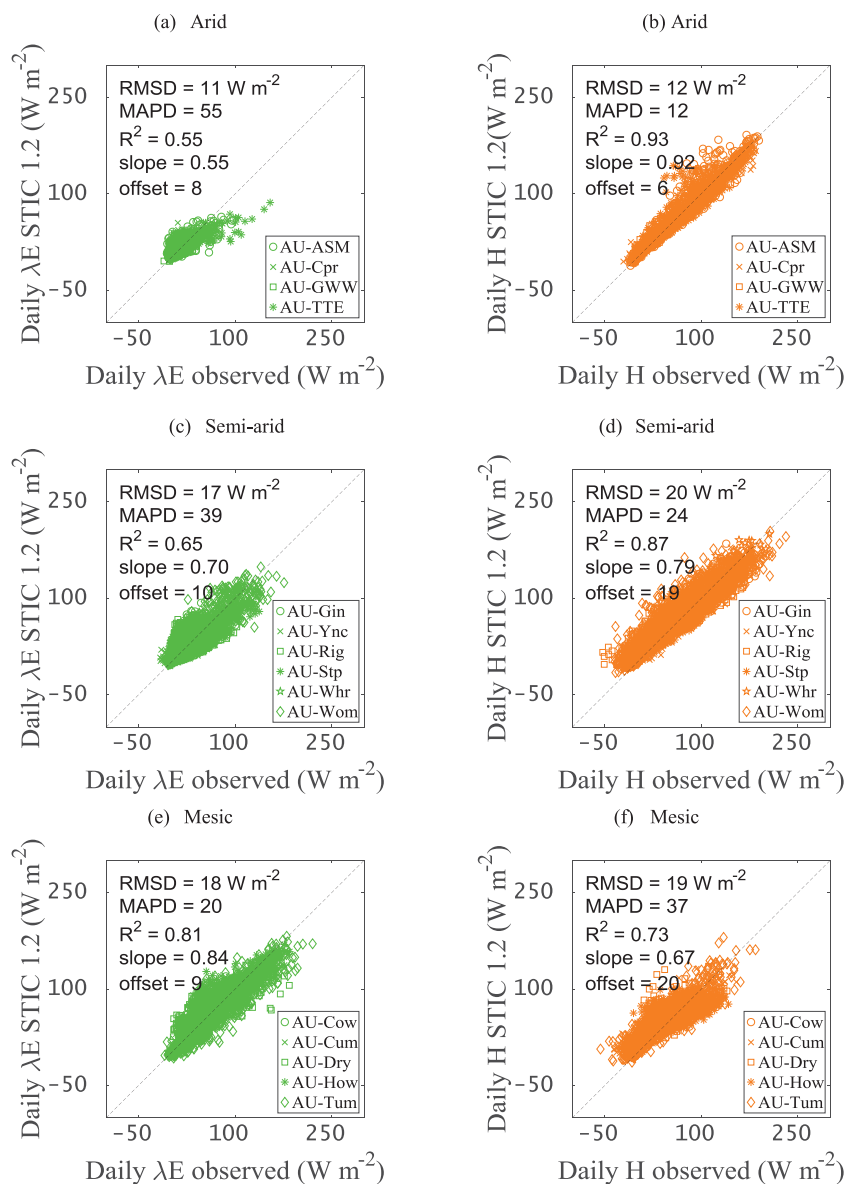


**Figure 4.** Comparison of daily (a, c, and e)  $\lambda E$  and (b, d, and f)  $H$  predicted by STIC1.2 with measured SEB flux components in ecohydrologically contrasting OzFlux ecosystems of three aridity classes (as defined in Table 1). Data from the sites falling under same aridity class are combined together.

were found between STIC1.2 and STIC1.0, whereas the differences were relatively lower (5–40%, 3–22%, and 5–18% in MAPD; 3–10 W m<sup>-2</sup>, 2–8 W m<sup>-2</sup>, and 4–18 W m<sup>-2</sup> in RMSD) between STIC1.2 and STIC1.1 (Figure A1). Statistical metrics of individual site-year is given in Table A2 with description in Appendix A1.

**5.2. Effects of  $T_R$  and Environmental Variables on the Performance of STIC1.2 in Different Ecosystems**  
 Sensitivity analysis revealed that the relative change in  $\lambda E$  error is inversely related to the relative change in  $T_R$ , thus a 10% reduction in  $T_R$  can lead up to 50% increase in percent  $\lambda E$  error for these ecosystems (Figures 6a, 6c, and 6e) (Table 3). Maximum sensitivity of  $\lambda E$  to  $T_R$  was found for arid and semi-arid ecosystems with significant correlations of ( $-0.35$ ) to ( $-0.92$ ) and ( $-0.30$ ) to ( $-0.35$ ) ( $p < 0.05$ ) for soil moistures above  $0.05 \text{ m}^3 \text{ m}^{-3}$  and  $0.10 \text{ m}^3 \text{ m}^{-3}$  (Table 3), respectively. In the mesic ecosystems, the sensitivity of  $\lambda E$  errors to  $T_R$  was relatively uniform across all the ranges of soil moisture ( $r = (-0.26)$  to ( $-0.29$ ),  $p < 0.05$ ) and  $E_p/\phi$  ( $r = (-0.27)$  to ( $-0.31$ ),  $p < 0.05$ ) (other than conditions of extremely high evaporative potential) (Table 3). In arid and semi-arid ecosystems, the sensitivity of the  $\lambda E$  error to  $T_R$  was confounded due to  $E_p/\phi$  (Figures 6a and 6c) (also evident from the principal component analysis described below).

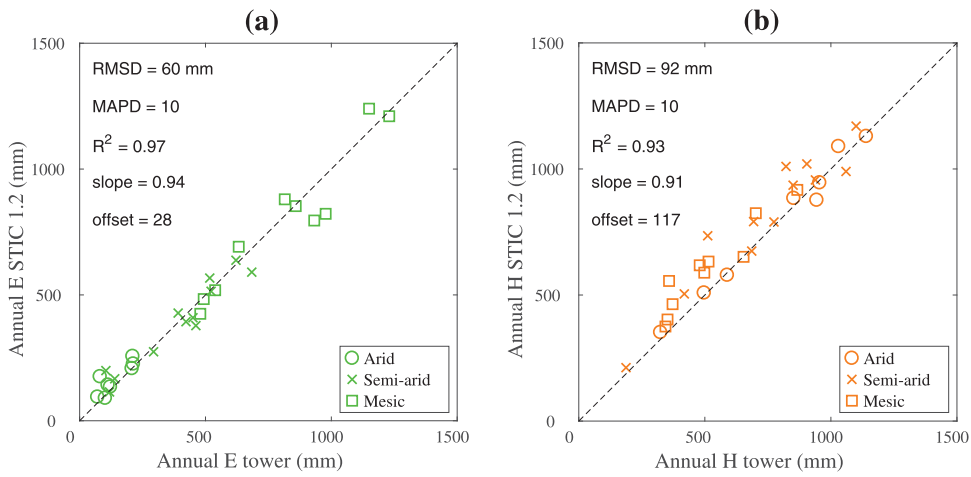


**Figure 5.** (a and b) Validation of STIC1.2 estimates of annual  $E$  and  $H$  against EC tower measurements. These are the annual sum of  $E$  and  $H$  for years 2013 and 2014 at each of the flux tower sites categorized according to their aridity class as defined in Table 1.

Principal component regression (PCR) of  $\Delta_{\lambda E}$  versus  $T_R$  and environmental variables ( $\phi$ ,  $D_A$ , and  $u$ ) revealed  $T_R$ ,  $D_A$ , and  $\phi$  to be the first principal component (PC1) affecting  $\Delta_{\lambda E}$  variance in all the ecosystems (Figures 6b, 6d, and 6f). However, the relative effect of  $T_R$  in conjunction with different environmental factors in controlling the variance of  $\Delta_{\lambda E}$  varied among ecosystems. Maximum PC1 loading was found for  $T_R$  and  $D_A$  followed by  $\phi$  in arid and semi-arid ecosystems (Figures 6b and 6d) where their correlation with  $\Delta_{\lambda E}$  varied between 0.70 and 0.75 ( $T_R$ ), 0.65 and 0.70 ( $D_A$ ) and 0.50 and 0.55 ( $\phi$ ), respectively (Figures 6b and 6d). Contrarily, in the mesic ecosystem, all the three variables had equal loadings (correlation 0.50) with  $\Delta_{\lambda E}$  variance in PC1 axis (Figure 6f). The effects of wind speed ( $u$ ) on the  $\Delta_{\lambda E}$  variance was reflected in the second principal component (PC2) axis with correlation varying from 0.55 to 0.75. The residual errors in sensible heat flux ( $\Delta_H$ ) showed similar behavior of the  $\Delta_H$  variance as the variance of  $\Delta_{\lambda E}$  against  $T_R$  and environmental variables (not shown).

### 5.3. Relationship between Ecohydrological Conditions and $T_R$ in Determining Errors and Variability of SEB Flux Components Predicted by STIC1.2

The scatter between MAPD and ecohydrological indicators in Figure 7 shows opposite relationships for  $\lambda E$  and  $H$ . Annual  $E/R_N$  ratio and  $\epsilon$  had the strongest impacts on the MAPD of both fluxes. As evident from the slopes of the regression lines, 1% increase in  $\epsilon$  was found to cause approximately 17% decrease (15% increase) in MAPD $_{\lambda E}$  (MAPD $_H$ ) (Figure 7a). An increase of 10% in  $E/R_N$  would cause a 76% decrease and 55% increase in MAPD $_{\lambda E}$  and MAPD $_H$ , respectively (Figure 7c). A systematic increase in MAPD $_{\lambda E}$  was found with increasing  $cV_\theta$ , where a 10% increase in  $cV_\theta$  resulted in 34% increase in MAPD $_{\lambda E}$  (Figure 7b). However, the impact of variation in  $\theta$  was approximately 50% less for the accuracy of predicted  $H$ , as evident from the slope of the regression line (slope = 0.19) (Figure 7b). Interestingly, a logarithmic increase in MAPD $_{\lambda E}$  was found with increasing climatic dryness (Figure 7d). MAPD $_{\lambda E}$  varied from 18 to 30% for  $E_p/P$  ratio of 0 to 2.5 and it progressively increased from 55% to 100% when  $E_p/P$  ratio exceeded 5 (Figure 7d).

The scatter plots of monthly variances in predicted versus observed  $\lambda E$  and  $H$  ( $\sigma^2_{\lambda E}$  and  $\sigma^2_H$ ) revealed the capacity of STIC1.2 to explain 88–90% of the observed flux variances in a broad range of aridity conditions (Figures 8a and 8b). The correlation matrix of the residual variance in the fluxes ( $\Delta\sigma^2_{\lambda E} = \sigma^2_{\lambda E}$  STIC1.2 –  $\sigma^2_{\lambda E}$  observed and  $\Delta\sigma^2_H = \sigma^2_H$  STIC1.2 –  $\sigma^2_H$  observed) against a host of ecohydrological and meteorological variables revealed the absence of any strong systematic relationship between  $\Delta\sigma^2_{\lambda E}$  and  $\sigma^2_{TR}$ ,  $\sigma^2_\theta$ ,  $\sigma^2_P$  ( $r = \pm 0.2$ ) (Figure 8c). For  $H$ , the similar analysis revealed 20–40% correlation between  $\Delta\sigma^2_H$  and  $\sigma^2_{TR}$ ,  $\sigma^2_{TA}$  (Figure 8d).

## 6. Discussion

Section 6.1 describes SEB flux prediction errors for STIC1.2 in the context of uncertainty in the relationship between  $T_R$  and aggregated moisture availability by evaluating the relationship between  $M$ ,  $T_R$ , and the conductances, and thereby assessing the role of conductances estimates on residual  $\lambda E$  error. This section also highlights the impact of SEB closure correction errors in MAPD and systematic RMSD of the predicted fluxes.

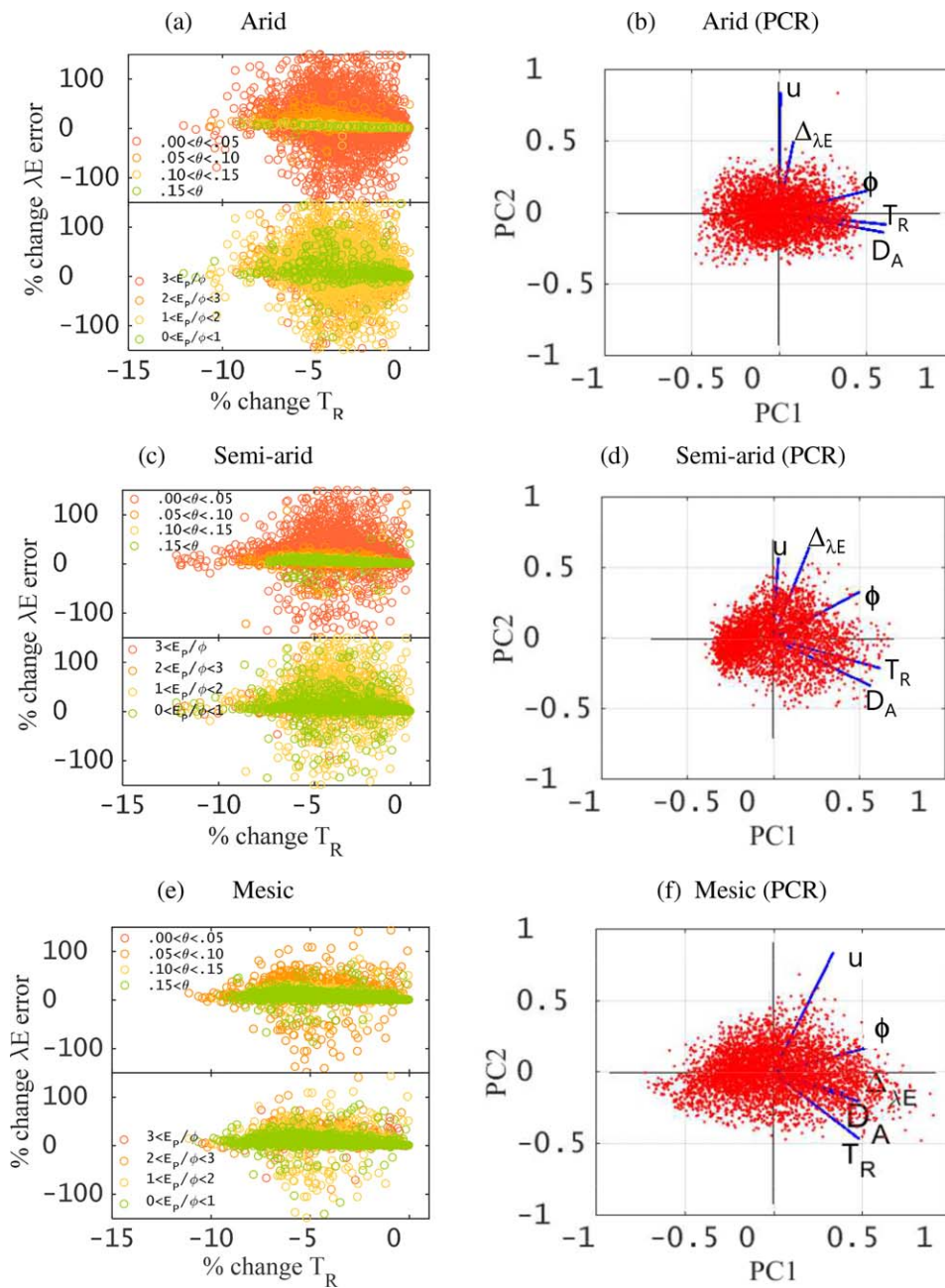


**Figure 6.** (a, c, and e) Scatter plots showing relative change in  $\lambda E$  errors due to relative change in  $T_R$  in three ecosystems of contrasting aridity. (b, d, and f) Loadings of Principal Component Regression (PCR) between residual error in STIC1.2  $\lambda E$  ( $\Delta_{\lambda E}$ ) with  $T_R$  and environmental variables showing the contribution of each principal component in explaining the variance of the residual  $\lambda E$  error. Half-hourly data are used for this analysis.

Section 6.2 discusses how the collective role of  $T_R$  and environmental variables affect the predictive errors in STIC1.2. Lastly, section 6.3 discusses the link between  $T_R$  and ecohydrological conditions in determining the error and variability of STIC1.2-based SEB flux predictions.

### 6.1. What is the Performance of STIC1.2 When Evaluated With High Temporal Resolution Data Across an Aridity Gradient in Australia?

#### 6.1.1. Role of Uncertain Relationship Between $M$ and $T_R$

Evaluation of STIC1.2-derived SEB fluxes at 15 Ozflux sites of broad aridity classes revealed relatively large differences between predicted and observed  $\lambda E$  in the arid ecosystems as compared to the semi-arid and

**Table 3**

Sensitivity of  $\lambda E$  Error to  $T_R$  in Three Different Types of OzFlux Ecosystems, as Shown by the Cross Correlation Between the Change in %  $\lambda E$  Error and % Change in  $T_R$  for a Range of Soil Moisture and Potential Evaporation-Net Available Energy Ratio

$\theta$ and $E_p/\phi$ criteria	Class	Correlation between relative change in $\lambda E$ error (%) and relative change in $T_R$ (%)		
		Arid	Semi-arid	Mesic
$\theta$ ( $m^3 m^{-3}$ )	$0 < \theta < 0.05$	-0.17	-0.14	<b>-0.29</b>
	$0.05 < \theta < 0.10$	<b>-0.38</b>	-0.18	<b>-0.29</b>
	$0.10 < \theta < 0.15$	<b>-0.35</b>	<b>-0.30</b>	<b>-0.23</b>
	$0.15 < \theta$	<b>-0.92</b>	<b>-0.36</b>	<b>-0.29</b>
$E_p/\phi$ ratio	$3 < E_p/\phi$	-0.16	-0.10	-0.09
	$2 < E_p/\phi < 3$	-0.18	-0.19	<b>-0.27</b>
	$1 < E_p/\phi < 2$	-0.17	-0.17	<b>-0.28</b>
	$0 < E_p/\phi < 1$	-0.14	-0.14	<b>-0.31</b>

Note. The bold values are moderate to high correlation and highly significant ( $p < 0.05$ ), whereas the non-bold values are low correlation and significant ( $p < 0.05$ ).

mesic ecosystems. Uncertainty in the relationship between  $T_R$  and aggregated moisture availability ( $M$ ) could be a considerable source of error in the predictive power of STIC1.2 in the water-limited ecosystems. In STIC1.2,  $M$  is modeled as a fraction of the dewpoint temperature difference between evaporating front and atmosphere ( $T_{OD} - T_D$ ) and of infrared temperature—dewpoint differences between surface to atmosphere ( $T_R - T_D$ ). These two factors were weighted by two different slopes of saturation vapor pressure-temperature relationships ( $s_1$  and  $s_2$ ; equation (S26)) (Mallik et al., 2016). This implies that for constant available moisture, this fraction is constant. However, even for varying  $\phi$ ,  $D_A$ , and  $T_A$ , constant moisture availability does not imply invariant  $(T_{OD} - T_D)/(T_R - T_D)$  because a wet surface has a different sensitivity to these variables than a dry surface with limited surface conductance. Due to  $\phi - D_A - T_R$  feedbacks (Zhang et al., 2014),  $T_{OD} - T_D$  can actually decrease with increasing  $T_R$ ,  $\phi$ , and  $D_A$ , whereas  $T_R - T_D$  would increase. In this context, estimation of  $T_{OD}$  plays a critical role in arid and semi-arid environments, which further requires sound estimation of  $s_1$ . From the definition of  $s_1$  [ $(e_0 - e_A)/(T_{OD} - T_D)$ ],  $e_0 \rightarrow e_A$  and  $s_1 \rightarrow 0$  for an extremely dry surface with insignificant evaporation. In the present

case, the estimates of  $s_1$  as a function of  $T_D$  tend to be higher than the possible  $s_1$ -limits in water-limited environments, which is likely to introduce errors in  $T_{OD}$  estimation (through supporting information equation (S27)). Overestimation of  $s_1$  would also lead to an overestimation of  $M$  (through the denominator in supporting information equation (S26)), thus leading to overestimation of the conductances and  $\lambda E$ . As seen in Figures 9a, 9c, and 9d, the relationship between  $M$  and  $T_R$  is very strong for low magnitudes of  $M$  ( $M < 0.025$  for arid ecosystem;  $M < 0.10$  for semi-arid and mesic ecosystems), and a significantly strong

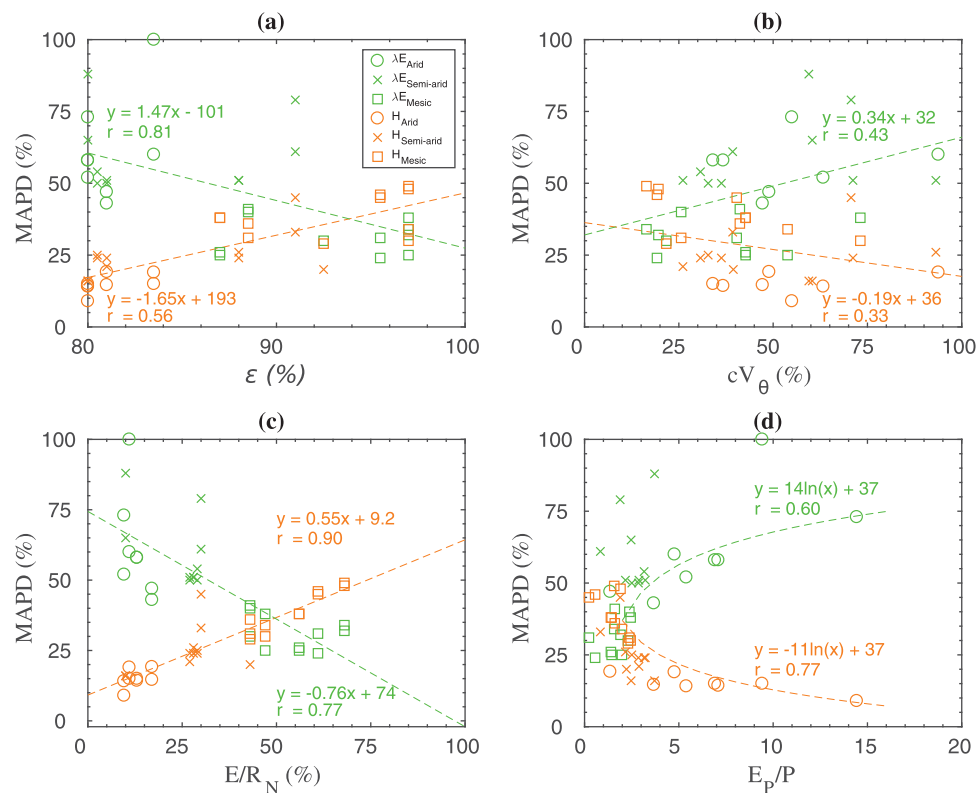


**Figure 7.** (a–d) Scatters between MAPD in daily  $\lambda E$  and  $H$  versus ecohydrological and land surface variables combining data from 15 OzFlux ecosystems representing three broad aridity classes as described in Table 1.

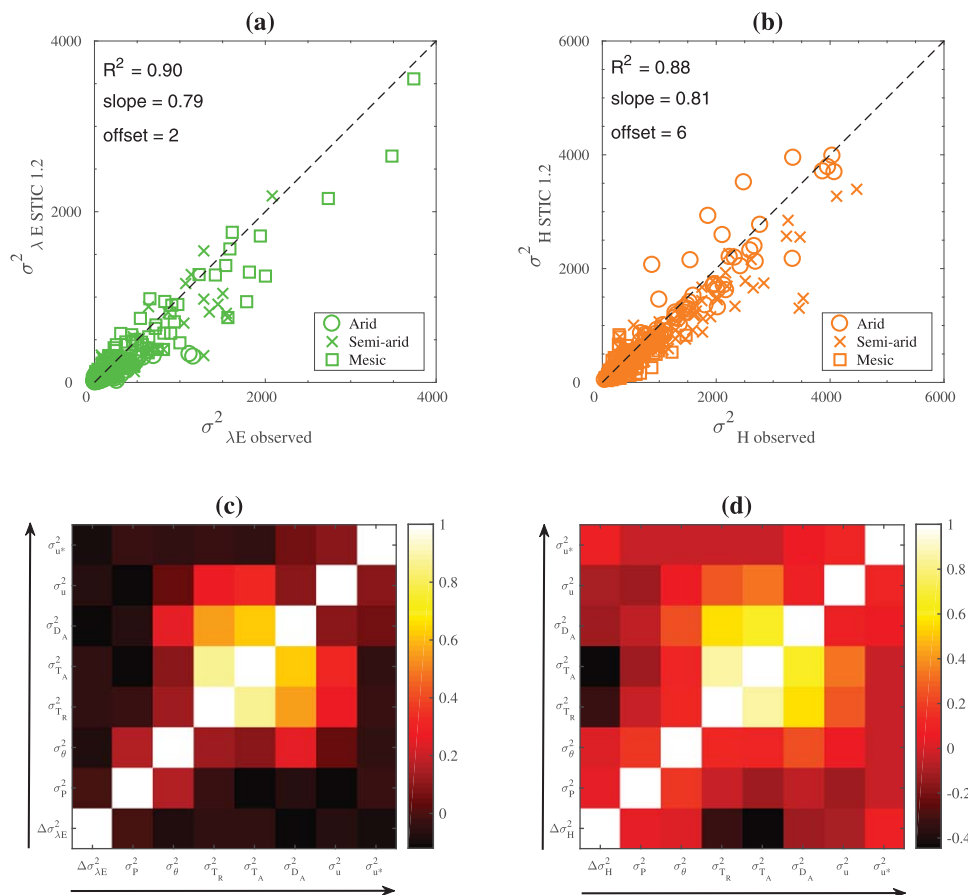


**Figure 8.** (a and b) Scatters of monthly variance of STIC1.2 versus observed  $\lambda E$  ( $\sigma^2_{\lambda E}$ ) and  $H$  ( $\sigma^2_H$ ) in contrasting OzFlux ecosystems representing three broad aridity classes as defined in Table 1. (c and d) Correlation matrix showing the relationship between the residual variances in  $\lambda E$  ( $\partial \sigma^2_{\lambda E} = \sigma^2_{\lambda E \text{ STIC1.2}} - \sigma^2_{\lambda E \text{ observed}}$ ) and  $H$  ( $\partial \sigma^2_H = \sigma^2_{H \text{ STIC1.2}} - \sigma^2_{H \text{ observed}}$ ) versus ecohydrological and meteorological variables.

relationship is also evident between  $g_C/g_A$  versus  $M$  ( $r = 0.81\text{--}0.88$ ;  $p < 0.05$ ) in all the ecosystems when the surface is substantially dry ( $M < 0.15$ ).  $g_C/g_A$  ratios tend to be invariant with increasing moisture availability in the mesic ecosystems ( $M > 0.25$ ; Figure 9e). Therefore, critical errors could be introduced in  $\lambda E$  retrieval under dry surface conditions due to the strong association between  $M$  and  $T_R$ , and dependence of the conductances on  $M$ . Residual error analysis of  $\lambda E$  versus both the conductances revealed  $\lambda E$  error to be fairly correlated with  $g_A$  and  $g_C$  in the sparsely vegetated arid and semi-arid ecosystems (Figures 9b and 9d) ( $r = 0.30\text{--}0.40$ ,  $p < 0.05$ ;  $r = 0.28\text{--}0.32$ ,  $p < 0.05$ ). There was a general tendency to overestimate  $\lambda E$  when  $g_C$  was very low, which was eventually reduced with increasing  $g_C$ . Residual  $\lambda E$  error appears to be heteroscedastic with  $g_A$ , which signifies unequal variability of  $\lambda E$  error across a range of  $g_A$ . A weak relationship between residual  $\lambda E$  error and conductances was found in the mesic ecosystem (Figure 9f), resulting in small predictive errors in  $\lambda E$  for this ecosystem.

Significantly lower errors in predicting  $H$  than  $\lambda E$  might be the result of partial compensation of  $g_A/g_C$  in both numerator and denominator of the PM formulation for  $H$  (equation (4b)) (Winter & Eltahir, 2010). In our study,  $g_C$  showed much more variability as a function of  $T_R$  ( $r = 0.72\text{--}0.74$ ; 1% change in  $T_R$  would lead to 5.2–7.5% change in  $g_C$ ) than did  $g_A$  with  $T_R$  ( $r = 0.26\text{--}0.65$ ; 1% change in  $T_R$  would lead to 1.6–2% change in  $g_A$ ) (Figure 10), suggesting that error in  $g_C$  was larger than error in  $g_A$ . Compensation of conductance errors in computing  $H$  (equation (4b)) might have resulted in substantial compensation of  $H$  errors in all the ecosystems. By contrast, combined uncertainty due to  $g_A$  in the numerator of equation (4a) with uncompensated  $g_A/g_C$  in the denominator of equation (4a) (Mallick et al., 2015; Winter & Eltahir, 2010) resulted large disagreements in measured and modeled  $\lambda E$  for the arid and semi-arid ecosystems where  $\lambda E$  was small.

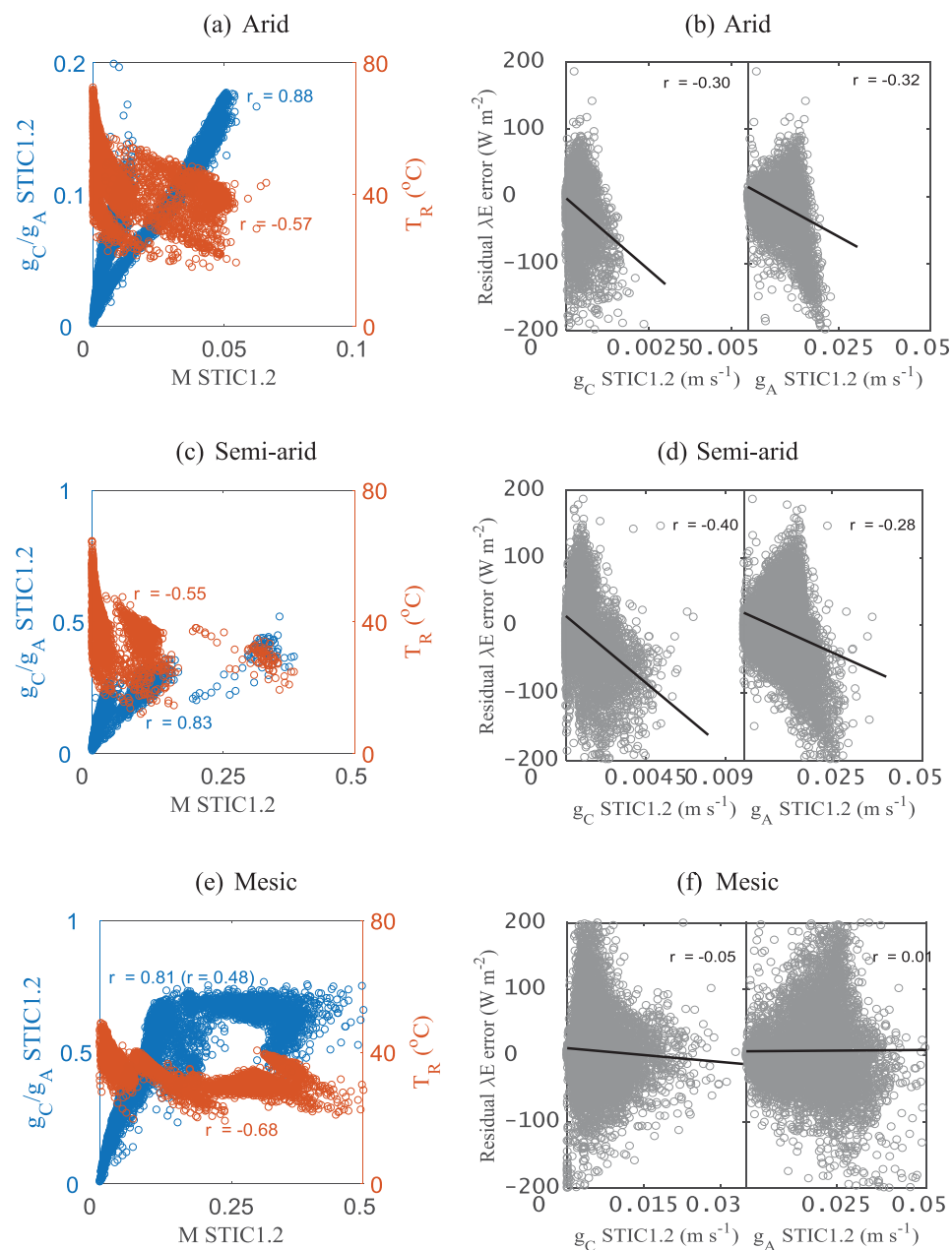


**Figure 9.** (a, c, and e) Scatter plots showing the relationship between  $g_C/g_A$  versus  $M$  and  $M$  versus  $T_R$  as modeled in STIC1.2 for different ecosystem types. (b, d, and f) Scatter plots showing how the residual  $\lambda E$  error in STIC1.2 is affected by  $g_C$  and  $g_A$  for different types of aridity classes.

#### 6.1.2. Role of SEB Closure on Statistical Metrics

Differences between STIC1.2 versus observed  $\lambda E$  may be partly attributed to the BREB-closure correction of  $\lambda E$  observations. Although Bowen ratio correction forces SEB closure, in the arid and semi-arid ecosystems major corrections are generally observed in  $H$ , whereas  $\lambda E$  is negligibly corrected (Chávez et al., 2005). Significant correlations are found between the  $\lambda E$  error statistics and BREB-closure corrections ( $r = 0.60$  for MAPD in Figure 11a,  $r = 0.66$  for  $RMSDs^2/RMSD^2$  in Figure 11b). In majority of the arid and semi-arid sites, high MAPD and  $RMSDs^2/RMSD^2$  in  $\lambda E$  ( $>50\%$ ) was associated with low percent of closure correction in  $\lambda E$  (12–20%) (Figures 11a and 11b). Both the error metrics were relatively high when modeled  $\lambda E$  was compared against RES-closure-based  $\lambda E$  observations; however, RES-closure revealed a substantially weaker relationship between errors and percent closure corrections than in BREB-closure (Figures 11c and 11d).

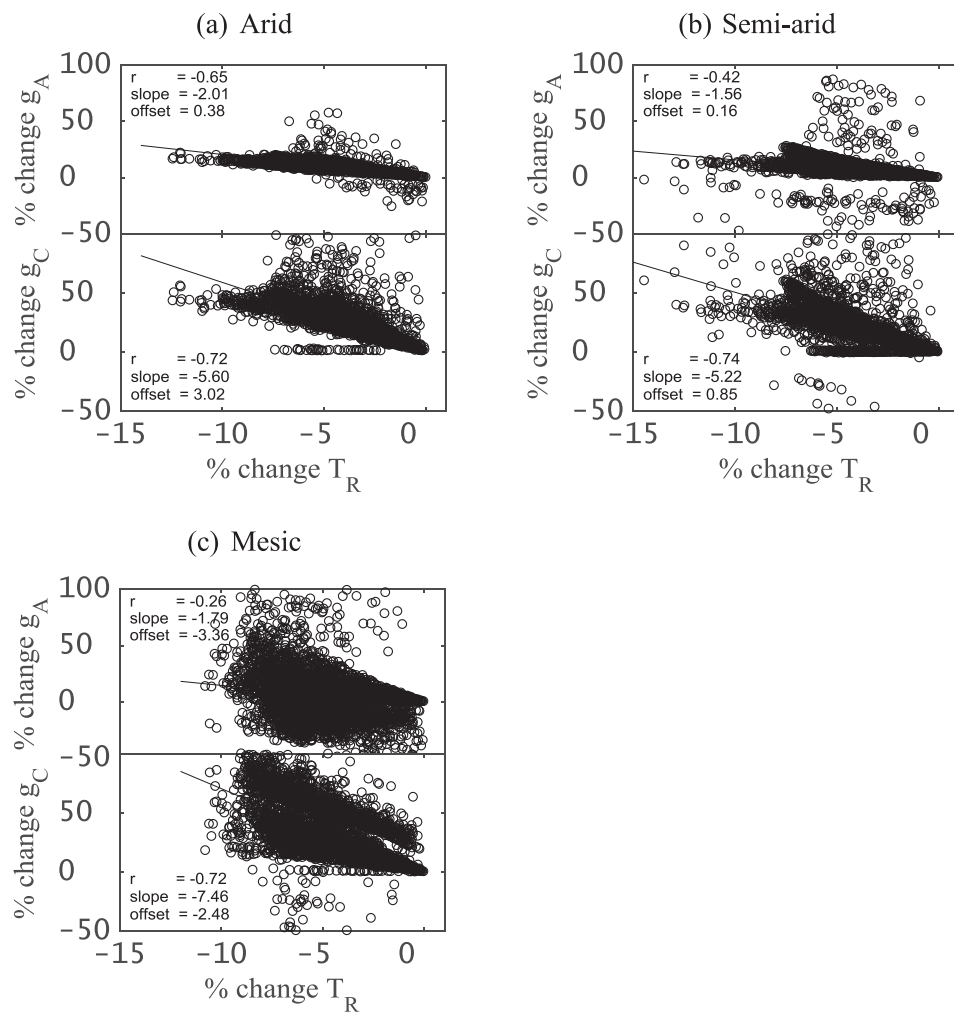


**Figure 10.** Scatter plots showing the sensitivity of  $g_A$  and  $g_C$  to  $T_R$  as modeled in STIC1.2 in three different classes of ecosystems. This shows the relative change in the individual conductances due to the relative change in  $T_R$ .

BREB-closure correction was found to fail under hot, dry conditions in some previous studies. This is due to the combination of extremely high evaporative potential and sensible heat entrainment from boundary layer desaturating the surface and causing the surface-to-air vapor pressure gradient to reverse (Mallick et al., 2014b; McHugh et al., 2015; Perez et al., 1999), a condition that prevails in the arid and semi-arid ecosystems during most part the year. The assumption of scalar similarity for heat and water vapor is violated in these conditions and  $g_A$  of heat flux can be two to three times higher than  $g_A$  of the water vapor flux (Katul et al., 1995). For the RES-closure, additional uncertainty in  $\lambda E$  might be introduced due to neglecting subsurface heat sink in  $G$  measurements (Heitman et al., 2010), which themselves can have errors of 18–66% (Ochsner et al., 2006). Similar analysis of  $H$  revealed relatively low overall correlation ( $r = 0.41$ ) between MAPD of predicted  $H$  and SEB closure (Figures 11e and 11f), with a tendency of high MAPD in mesic sites due to overcorrection of  $H$ . This is due to the fact that  $g_A$  responsible for  $H$  might be lower than  $g_A$  of  $\lambda E$  in mesic ecosystems and the assumption of scalar similarity for heat and water vapor may not be true. For a similar reason, the use of Bowen ratio approximations in the state equation of  $T_0$  in STIC1.2 might also be responsible for additional error propagation in all the three ecosystems.

## 6.2. How Do $T_R$ and Associated Environmental Variables Affect the Performance of STIC1.2 in Different Ecosystems?

The relationship between the relative change in  $\lambda E$  error with the relative change in  $T_R$  above a threshold soil moisture content in arid and semi-arid ecosystems (Figures 6a, 6c, and 6e; Table 3) indicates the critical

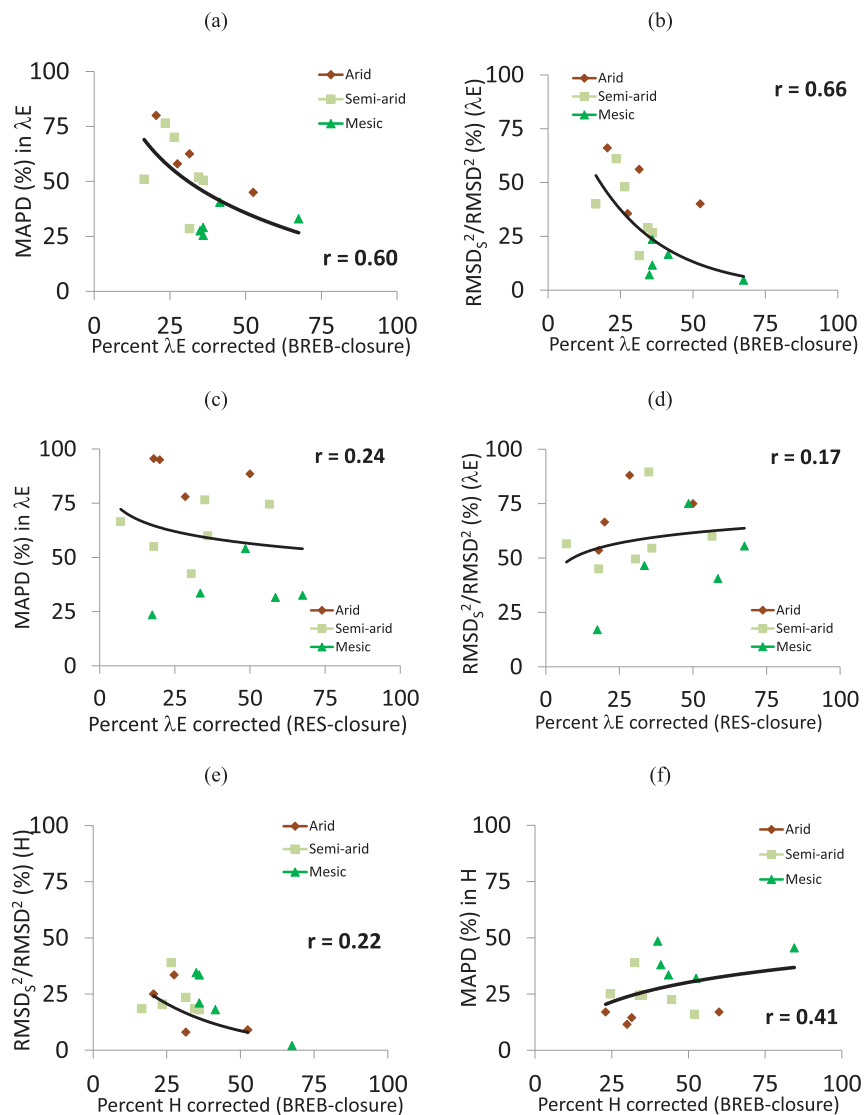


**Figure 11.** (a–d) Scatters of MAPD and  $\text{RMSD}_s^2/\text{RMSD}^2$  in half-hourly  $\lambda E$  predicted by STIC1.2 versus average percent of BREB-closure corrected  $\lambda E$  and RES-closure corrected  $\lambda E$  measured with the EC method. (e and f) Scatters of MAPD and  $\text{RMSD}_s^2/\text{RMSD}^2$  in half-hourly  $H$  predicted by STIC1.2 versus average percent of BREB-closure corrected  $H$  measured with the EC method. Data from 15 OzFlux sites falling under three classes of contrasting aridity (as in Table 1) are grouped. Relative  $\lambda E$  and  $H$  correction (in percent) is computed as, % $\lambda E$  correction =  $100 * (\lambda E_{\text{corrected}} - \lambda E_{\text{uncorrected}}) / \lambda E_{\text{uncorrected}}$  and % $H$  correction =  $100 * (H_{\text{corrected}} - H_{\text{uncorrected}}) / H_{\text{uncorrected}}$ . Here  $\lambda E_{\text{corrected}}$  and  $H_{\text{corrected}}$  are the Bowen ratio corrected  $\lambda E$  ( $\lambda E_{\text{uncorrected}}$ ) and  $H$  ( $H_{\text{uncorrected}}$ ) observations.

role of uncertainty in  $T_R$ -soil moisture relationship in STIC1.2 and the role of  $M$  in controlling  $g_C/g_A$  and resultant  $\lambda E$  errors in the water-limited ecosystems, as discussed previously. As further evident from Figures 6b, 6d, and 6f, while the accumulated effects of  $T_R$  and  $D_A$  were predominant in explaining  $\Delta_{\lambda E}$  variance in arid and semi-arid ecosystems, the influence of  $\phi$  was comparable to  $T_R$  and  $D_A$  in explaining  $\Delta_{\lambda E}$  variance in the mesic ecosystems. Since  $T_R$  controls the atmospheric humidity profile by constraining soil moisture,  $g_C$  and transpiration;  $T_R$  and  $D_A$  have stronger autocorrelation in arid and semi-arid ecosystems as compared to the mesic ecosystems (Abdi et al., 2017; Crago & Qualls, 2014); and  $\lambda E$  is mainly limited by combination of these two surface and atmospheric moisture variables. This explains the dominant role of  $T_R$  and  $D_A$  in controlling the maximum  $\Delta_{\lambda E}$  variance as reflected in the high correlation (0.65–0.75) in the first principal component (PC1) axis of arid and semi-arid ecosystems (Figures 6b and 6d). In contrast,  $E$  in mesic ecosystems is constrained by  $T_R$ ,  $\phi$ , and  $D_A$ ; and all the three variables had accumulated impact in explaining the relative error

change in  $\lambda E$  (Table 3 and Figure 6e) and  $\Delta_{\lambda E}$  variance as seen in the PC1 axis in this ecosystem (Figure 6f). Since PC1 had the highest total variance in all the ecosystems, its variables are the most important in determining the predictive errors in  $\lambda E$ . The effects of wind speed ( $u$ ) in explaining  $\Delta_{\lambda E}$  variance (as seen in PC2) might originate from some collinearity of  $u$  with net radiative heating,  $T_R$  and  $D_A$  as earlier reported by Mallick et al. (2016).

### 6.3. Is There an Association between Ecohydrological Conditions and $T_R$ in Determining the Errors and Variability of SEB Flux Components Predicted by STIC1.2?

Given the critical role of  $T_R$  in STIC1.2, the estimate of  $T_R$  is an additional source of error (through  $\varepsilon$ ) in predicted  $\lambda E$  and  $H$  for the individual study sites (Figure 7a) and the error is consequently propagated into the MAPD of  $\lambda E$  and  $H$  versus  $cV_\theta$ , annual  $E/R_N$ , and  $E_P/P$  relationships (Figures 7b–7d). Low annual  $E/R_N$  and high annual  $E_P/P$  are the indicators of water limitations, where low  $E$  is the result of low  $P$  and  $\theta$  despite an abundance of available energy in conjunction with high potential evaporative demand. Such water limitations make  $E$  very sensitive to soil moisture variations (Jarvis & McNaughton, 1986), thereby accelerating biophysical feedbacks on  $E$  (Mallick et al., 2016; Siqueira et al., 2008), and the rate of change of  $E$  becomes directly proportional to the canopy (or surface) conductance ( $g_C$ ) (Jarvis & McNaughton, 1986). Since our  $g_C$  estimates are inevitably constrained by  $T_R$  (through  $M$ ), accuracy of  $T_R$  is a key factor for enhancing  $E$  retrievals under these conditions.

Given  $\varepsilon$  appears in the denominator of the  $T_R$  retrieval equation,  $T_R$  is extremely sensitive to the uncertainties in  $\varepsilon$  (Hulley et al., 2012). Underestimation (overestimation) of  $T_R$  would lead to overestimation (underestimation) of  $M$ , which further leads to underestimation (overestimation) of  $g_A/g_C$  in the denominator of the PM model, causing the resultant SEB flux estimations to become uncertain. Careful handling of diurnal variations of infrared  $\varepsilon$  is therefore essential for deriving accurate surface skin temperature (Hulley et al., 2012; Li et al., 2007). Substantial diurnal variations in  $\varepsilon$  are found in arid and semi-arid ecosystems due to the influence of soil moisture ( $\theta$ ) (Hulley et al., 2010; Masiello et al., 2014). For low values of  $\theta$ , the rate of change of  $\varepsilon$  per unit change of  $\theta$  (i.e.,  $\partial\varepsilon/\partial\theta$ ), at wave numbers of reststrahlen absorption is considerably large (Masiello et al., 2014; Mira et al., 2007);  $\partial\varepsilon \approx 0.05$  per  $\partial\theta$  of  $0.01 \text{ kg kg}^{-1}$ . Consequently, exclusion of sub-daily and seasonal variation of  $\varepsilon$  in the  $T_R$  estimation is evident in MAPD of  $\lambda E$  versus  $\varepsilon$  scatter plots (Figure 7a).

Despite the absolute differences between the predicted and observed SEB fluxes, very good agreement between the flux variances (Figures 9a and 9b) indicates the ability of STIC1.2 to capture the radiation and water driven variabilities in SEB fluxes from mesic to arid ecosystems. The correlation of  $\pm 12\text{--}15\%$  between  $\Delta\sigma_{\lambda E}^2$  and  $\sigma_\theta^2$ ,  $\sigma_P^2$ , and  $\sigma_{TR}^2$  (Figure 9c) is a result of aforementioned (section 6.1)  $T_R$  uncertainties, in conjunction with SEB closure correction errors of EC  $\lambda E$  observations in arid and semi-arid environments. Besides, the negative relationship ( $r = -0.20$ ) between  $\Delta\sigma_{\lambda E}^2$  ( $\sigma_{\lambda E}^2$  STIC1.2 –  $\sigma_{\lambda E}^2$  observed) versus  $\sigma_{u^*}^2$  is most likely associated with the collinearity between wind shear and  $T_R$ ,  $D_A$ , and  $\phi$  (also reported in Mallick et al., 2016) as described in section 6.2. Nearly zero correlation between  $\Delta\sigma_H^2$  with ecohydrological variances further indicates that  $H$  was predominant in water-limited regions, and sensible heat flux is the primary pathway by which ecohydrological variances induces variations in atmospheric variables and consequently affects the boundary layer growth (Koster et al., 2015). This was also supported by 40% correlation between  $\Delta\sigma_H^2$  and  $\sigma_{TA}^2$ . Also the absence of a relationship between  $\Delta\sigma_H^2$  and  $\sigma_u^2$  indicates that the exclusion of wind speed from STIC1.2 (see equations (5)–(8)) does not significantly affect the SEB flux estimates. This error characterization in a broad range of ecohydrological conditions also indicated that in the ecosystems with low annual evaporative index ( $E/R_N$ ) and very high climatic dryness index ( $E_P/P$ ), the thermal component of the SEB fluxes (i.e.,  $H$ ) is dominant and should be given emphasis to assess model performance (Dirmeyer, 2011; García et al., 2008).

The overall RMSD of 25–61 and 11–37  $\text{W m}^{-2}$  in half-hourly and daily SEB fluxes and the associated statistical metrics are comparable with the results reported in a host of SEB modeling studies that uses empirical sub-models to parameterize the conductances. Using the two-source energy balance model (TSEB) (Norman et al., 1995), some recent studies have reported RMSD to the order of 72–135 and 52–131  $\text{W m}^{-2}$  in hourly  $\lambda E$  and  $H$  for a semi-arid grassland in Spain (Kustas et al., 2016), 95–166  $\text{W m}^{-2}$  in hourly  $\lambda E$  (Song et al., 2016) to 45–50  $\text{W m}^{-2}$  in daily  $\lambda E$  for semi-arid irrigated cotton in Texas and Arizona (Colaizzi et al., 2014; French et al., 2015), and 50–59  $\text{W m}^{-2}$  in hourly  $\lambda E$  for irrigated maize in China (Song et al., 2016). A variant of TSEB model (SPARSE model) is found to produce 43–47  $\text{W m}^{-2}$  in instantaneous  $\lambda E$  and 50–80  $\text{W m}^{-2}$  in

hourly  $\lambda E$  in Tunisia and Morocco (Boulet et al., 2015; Saadi et al., 2017). Considering the error statistics of state-of-the-art SEB models and their parameterization uncertainties (Timmermans et al., 2013); the performance of STIC1.2 indicates substantial potential of this model towards bridging thermal infrared sensing and physically-based evapotranspiration modeling. An intercomparison of STIC1.2 with other SEB models is beyond the scope of this manuscript. However, a recent study on regional evapotranspiration mapping demonstrated a comprehensive intercomparison of STIC1.2 with two other global models across an aridity gradient in the conterminous United States for contrasting rainfall years as well as on a wide variety of biomes (Bhattarai et al., 2018). The study revealed better performance of STIC1.2 as compared to the other models and also demonstrated the critical role of conductances and associated land surface parameterizations on the model errors, intermodel agreements, and disagreements.

A host of literatures reported measurement uncertainties in  $H$  and  $\lambda E$  to the order of  $\pm 15\text{--}20$  and  $\pm 35\text{--}50 \text{ W m}^{-2}$  (Masseroni et al., 2014; Wang et al., 2015). These uncertainties are associated with high magnitude of net radiation (Hollinger & Richardson, 2005), and with stochastic nature of turbulence (Hollinger & Richardson, 2005; Wang et al., 2015). Landscape heterogeneity may induce large scale turbulence which consequently leads to large  $H$  and  $\lambda E$  uncertainty in arid and semi-arid ecosystems (Wang et al., 2015). However, it is unlikely that the entire RMSD in  $\lambda E$  and  $H$  is attributable solely to the EC measurement uncertainties (Foken, 2008). As a result, the range of RMSD obtained between STIC1.2 and tower  $H$  and  $\lambda E$  is likely to be determined by the combination of structural uncertainties in STIC1.2 and SEB flux measurement uncertainties in the EC towers.

## 7. Conclusions

By integrating thermal infrared temperature into a combined structure of Penman-Monteith and Shuttleworth-Wallace framework we show the promise of a single-source box modeling approach towards bridging thermal infrared sensing and physically-based model to retrieve the energy-water fluxes. Analysis of STIC1.2 results in 15 eddy covariance sites across an aridity gradient in Australia led us to the following conclusions.

1. STIC1.2 overcomes the uncertainties in aerodynamic temperature and biophysical conductances parameterizations, and establishes a direct feedback of  $T_R$  on SEB fluxes, source/sink height temperature and vapor pressures, and the conductances. The efficiency of STIC1.2 to explain the variances of half-hourly to annual SEB fluxes across diverse biomes and ecohydrological settings in Australia indicates the skill of the model to capture the water-energy flux variabilities in hydrological extremes.
2. Uncertainty in the relationship between  $T_R$  and moisture availability ( $M$ ) is a considerable source of error in the predictive power of STIC1.2 in the water-limited ecosystems. Use of differential  $T_R$  observations (between sunrise and noontime) as a water stress constraint could potentially diminish the uncertainty in  $M$  and eventually SEB flux prediction errors in STIC1.2. Besides, the performance of STIC1.2 depends on rigorous surface emissivity ( $\epsilon$ ) corrections, particularly in arid and semi-arid ecosystems. Since  $\epsilon$  is sensitive to the soil water content variations, assuming a constant surface emissivity for retrieving  $T_R$  significantly affects the predictive skills of STIC1.2 in those ecosystems where substantial variations in soil moisture are observed. Spectrometer-based measurements representing appropriate footprint area around EC sites are needed to capture the diurnal variations in  $\epsilon$  for an improved  $T_R$  retrieval.
3. Disparities between predicted and observed  $\lambda E$  in arid semi-arid ecosystems also emerged due to the surface energy balance closure (SEB) correction errors of  $\lambda E$  observations. A robust SEB closure correction is needed for better interpretation of the predictive capacity of STIC1.2 in water-limited ecosystems.
4. In the arid ecosystems where evapotranspiration ( $E$ ) signal is small, the thermal component of the energy-water fluxes is predominant and sensible heat flux ( $H$ ) tends to be a better metric to test the skill of any physically-based model, and might be a favored water stress indicator. Simultaneously, in the semi-arid and mesic ecosystems, both  $E$  and  $H$  appear to be the better metric in detecting the water cycle variability, and STIC1.2 showed substantial promise to capture the magnitude and variabilities of these two most important energy-water cycle components across these broad aridity classes.
5.  $T_R$  is the most critical variable explaining the error variance of  $E$  in arid and semi-arid ecosystems, while both net available energy and  $T_R$  explain the error variance of  $E$  in mesic ecosystems. Effects of ecohydrological conditions in determining the predictive capacity of STIC1.2 are also associated with  $T_R$  and radiation driven SEB flux variability in the two ecohydrological extremes.

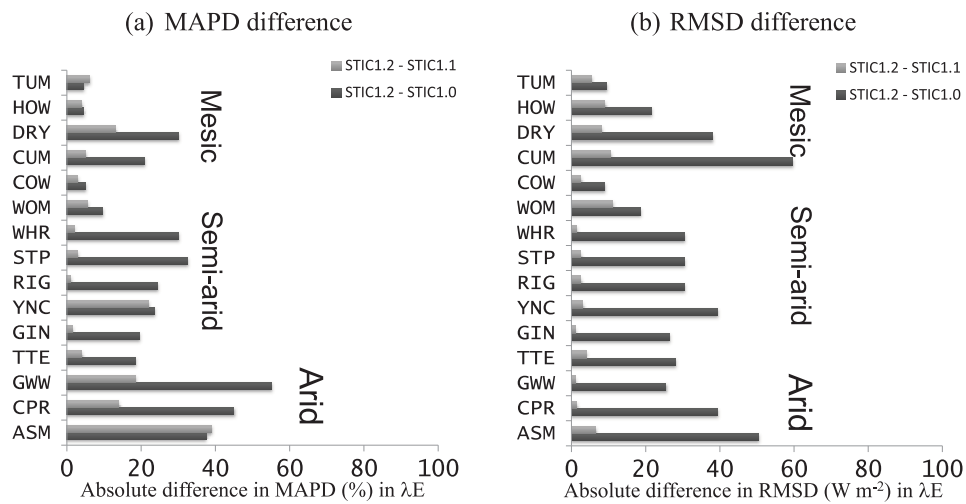


**Figure A1.** (a) Difference in MAPD (%) in  $\lambda E$  between STIC1.2 versus STIC1.1 and STIC1.0 for the 15 OzFlux sites, (b) Difference in RMSD ( $W m^{-2}$ ) in  $\lambda E$  between STIC1.2 versus STIC1.1 and STIC1.0 for the 15 OzFlux sites.

STIC1.2 is independent of any biome specific or leaf-scale empirical parameterizations of the conductances, which implies that it does not require any data on plant functional types or vegetation structure. This model is a valuable addition to the recent Australian energy and water exchange research initiative (OzEWEX), in particular to the WG2 (working group 2) that focuses on observations to evaluate and compare biophysical models and data products describing energy and water cycle variables. Given the significance of aerodynamic and canopy conductances in characterizing the land-atmosphere interactions, STIC1.2 can be used to study the ecohydrological feedbacks on land surface versus boundary layer interactions. With the availability of accurate  $T_R$  information from new MOD21 land surface temperature (Hulley et al., 2015), LANDSAT, recently launched Sentinel-3, or future missions with thermal sensors like HyspIRI, a successful application of STIC1.2 is expected for mapping regional-scale vegetation water use with special emphasis in the water-limited ecosystems.

## Appendix A

### A1. Intercomparison of STIC1.2 With STIC1.0 and STIC1.1

An intercomparison of STIC1.2 error statistics with the previous two versions of STIC (STIC1.0 and STIC1.1) revealed maximum improvement in the performance of STIC1.2 in arid and semi-arid ecosystems (as

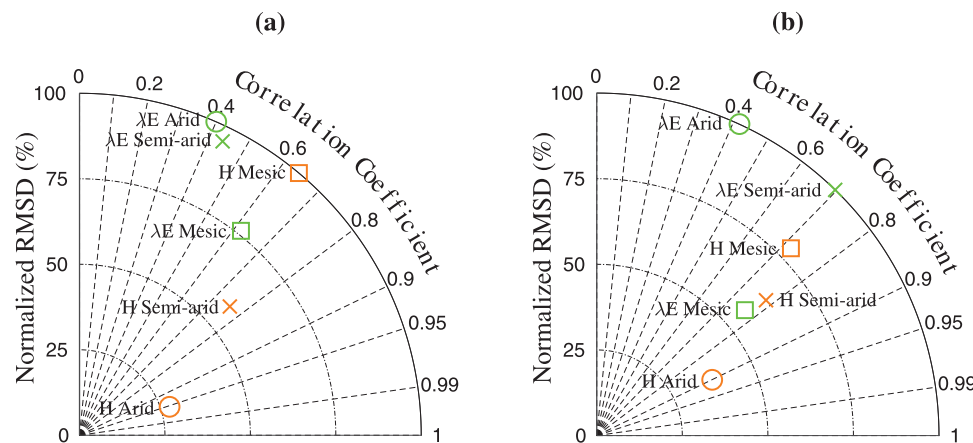


**Figure A2.** Taylor diagram of daily error statistics showing the normalized RMSD and correlation coefficient between observed and predicted  $\lambda E$  and  $H$  during (a) dry and (b) wet seasons of 2013–2014 in ecohydrologically contrasting OzFlux ecosystems of three aridity classes as defined in Table 1. Data from the sites falling under same aridity class are combined.

**Table A1**  
*Variables and Symbols and Their Description Used in the Present Study*

Variables and symbol	Description
$\lambda E$	Evapotranspiration (evaporation + transpiration) as latent heat flux ( $\text{W m}^{-2}$ )
$H$	Sensible heat flux ( $\text{W m}^{-2}$ )
$R_N$	Net radiation ( $\text{W m}^{-2}$ )
$G$	Ground heat flux ( $\text{W m}^{-2}$ )
$\phi$	Net available energy ( $\text{W m}^{-2}$ ) (i.e., $R_N - G$ )
$R_{S\downarrow}$	Downwelling shortwave radiation ( $\text{W m}^{-2}$ )
$R_{S\uparrow}$	Upwelling shortwave radiation ( $\text{W m}^{-2}$ )
$R_{L\downarrow}$	Downwelling longwave radiation ( $\text{W m}^{-2}$ )
$R_{L\uparrow}$	Upwelling longwave radiation ( $\text{W m}^{-2}$ )
$\varepsilon$	Thermal infrared surface emissivity
$T_A$	Air temperature ( $^{\circ}\text{C}$ )
$T_D$	Dewpoint temperature ( $^{\circ}\text{C}$ )
$T_R$	Radiometric surface temperature ( $^{\circ}\text{C}$ )
$T_0$	Aerodynamic temperature or source/sink height temperature ( $^{\circ}\text{C}$ )
$T_{0D}$	Dew-point temperature at the source/sink height ( $^{\circ}\text{C}$ )
$R_H$	Relative humidity (%)
$e_A$	Atmospheric vapor pressure at the level of $T_A$ measurement (hPa)
$D_A$	Atmospheric vapor pressure deficit at the level of $T_A$ measurement (hPa)
$e_S$	vapor pressure at surface (hPa)
$e_S^*$	Saturation vapor pressure at surface (hPa)
$e_0$	Vapor pressure at the source/sink height (hPa)
$e_0^*$	Saturation vapor pressure at the source/sink height (hPa)
$D_0$	Vapor pressure deficit at the source/sink height (hPa)
$u$	Wind speed ( $\text{m s}^{-1}$ )
$u^*$	Friction velocity ( $\text{m s}^{-1}$ )
$s$	Slope of saturation vapor pressure versus temperature curve ( $\text{hPa K}^{-1}$ ) (estimated at $T_A$ )
$s_1$	Slope of the saturation vapor pressure and temperature between ( $T_{SD} - T_D$ ) versus ( $e_0 - e_A$ ) (approximated at $T_D$ ) ( $\text{hPa K}^{-1}$ )
$s_2$	Slope of the saturation vapor pressure and temperature between ( $T_R - T_D$ ) versus ( $e_S^* - e_A$ ) ( $\text{hPa K}^{-1}$ )
$s_3$	Slope of the saturation vapor pressure and temperature between ( $T_R - T_{SD}$ ) versus ( $e_S^* - e_S$ ) (approximated at $T_R$ ) ( $\text{hPa K}^{-1}$ )
$s_0$	Slope of the saturation vapor pressure and temperature between ( $T_0 - T_A$ ) versus ( $e_0^* - e_A^*$ ) (approximated as $s$ ) ( $\text{hPa K}^{-1}$ )
$\kappa$	Ratio between ( $e_0^* - e_A$ ) and ( $e_S^* - e_A$ )
$E$	Evapotranspiration (evaporation + transpiration) as depth of water (mm)
$\lambda E_P$	Potential evaporation as flux ( $\text{W m}^{-2}$ )
$\lambda E_T^*$	Potential transpiration as flux ( $\text{W m}^{-2}$ )
$\lambda E_W$	Wet environment evaporation as flux ( $\text{W m}^{-2}$ )
$\lambda E_P^*$	Potential evaporation as flux according to Penman ( $\text{W m}^{-2}$ )
$\lambda E_{PM}^*$	Potential evaporation as flux according to Penman-Monteith ( $\text{W m}^{-2}$ )
$\lambda E_{PT}^*$	Potential evaporation as flux according to Priestley-Taylor ( $\text{W m}^{-2}$ )
$E_P$	Potential evaporation as depth of water (mm)
$E_P^*$	Potential evaporation as depth of water according to Penman (mm)
$E_{PM}^*$	Potential evaporation as depth of water according to Penman-Monteith (mm)
$E_{PT}^*$	Potential evaporation as depth of water according to Priestley-Taylor (mm)
$E_W$	Wet environment evaporation as depth of water (mm)
$g_A$	Aerodynamic conductance ( $\text{m s}^{-1}$ )
$g_M$	Momentum conductance ( $\text{m s}^{-1}$ )
$g_C$	Canopy (surface) conductance ( $\text{m s}^{-1}$ )
$g_{Cmax}$	Maximum canopy (surface) conductance ( $\text{m s}^{-1}$ ) (= $g_C/M$ )
$M$	Aggregated surface moisture availability (0–1)
$\lambda$	Latent heat of vaporization of water ( $\text{j kg}^{-1} \text{K}^{-1}$ )
$z_R$	Reference height (m)
$z_{0M}$	Effective source-sink height (roughness length) of momentum (m)
$z_{0H}$	Effective source-sink height (roughness length) of heat (m)
$d_0$	Displacement height (m)
$\gamma$	Psychrometric constant ( $\text{hPa K}^{-1}$ )

**Table A1.** (continued)

Variables and symbol	Description
$\rho$	Density of air ( $\text{kg m}^{-3}$ )
$c_p$	Specific heat of dry air ( $\text{MJ kg}^{-1} \text{K}^{-1}$ )
$\Lambda$	Evaporative fraction (unitless)
$\beta$	Bowen ratio (unitless)
$\alpha$	Priestley-Taylor parameter (unitless)
$\varrho$	Stefan-Boltzmann constant ( $5.670373 \times 10^{-8} \text{ W m}^{-2} \text{ K}^{-4}$ )

compared to mesic ecosystems) for both the SEB fluxes (Table A2). Statistical metrics of STIC1.0 and STIC1.1 (Table A2) revealed substantially higher RMSD ( $53\text{--}90 \text{ W m}^{-2}$  and  $36\text{--}49 \text{ W m}^{-2}$ ) and MAPD (91–100% and 60–100%), and lower  $R^2$  (0.23–0.64 and 0.28–0.67) as compared to STIC1.2 in arid ecosystems. In the semi-arid ecosystems, these statistics were  $59\text{--}91 \text{ W m}^{-2}$  and  $43\text{--}73 \text{ W m}^{-2}$  (RMSD); 31–100% and 28–100% (MAPD); and 0.19–0.84 and 0.21–0.84 ( $R^2$ ), respectively.

## A2. Dry Season Versus Wet Season Statistics in SEB Fluxes

The Taylor diagram (Figure A2) reveals overall lower percentage errors in  $H$  as compared to  $\lambda E$  in arid and semi-arid ecosystems during both dry and wet seasons (please see Table A3 for dry and wet season), with

**Table A2**

Error Statistics of Sub-daily  $\lambda E$  and  $H$  Derived With STIC1.0 and STIC1.1 in 15 EC Sites Covering Three Ecohydrologically Contrasting OzFlux Ecosystems of Different Aridity Classes as Defined in Table 1

Aridity class	Site name	STIC versions	$\lambda E$			$H$			RMSDs <sup>2</sup> /RMSD <sup>2</sup> (%)	
			RMSD ( $\text{W m}^{-2}$ )	$R^2$	MAPD (%)	RMSD ( $\text{W m}^{-2}$ )	$R^2$	MAPD (%)		
Arid (0 < AI < 0.2)	AU-ASM	STIC1.0	76–90	0.23–0.54	98–100	38–39	76–96	0.96–0.97	31–37	80–87
		STIC1.1	36	0.28–0.62	70–100	20–40	36	0.97–0.98	14–15	11–60
	AU-Cpr	STIC1.0	58–76	0.29–0.30	97–100	32–34	58–76	0.95–0.96	31–34	87–90
		STIC1.1	26–32	0.36–0.38	70–74	25–38	26–32	0.96–0.97	14–15	21–28
	AU-GWW	STIC1.0	53–66	0.46–0.56	91–100	19–35	53–66	0.92–0.95	28–30	69–82
		STIC1.1	33–35	0.53–0.60	60–67	37–59	33–35	0.94–0.96	14–20	6–8
	AU-TTE	STIC1.0	57–71	0.26–0.64	97–100	33–46	57–71	0.90–0.95	32–35	68–89
		STIC1.1	31–49	0.35–0.67	68–100	37–77	31–49	0.88–0.97	15–23	4–42
	AU-Gin	STIC1.0	77–83	0.50–0.51	66–77	16–20	77–83	0.86–0.89	33–34	71–77
		STIC1.1	54–55	0.53–0.55	53–54	40–53	54–55	0.90–0.91	24–26	14–15
Semi-arid (0.2 < AI < 0.5)	AU-Ync	STIC1.0	73–76	0.19–0.26	95–100	35–40	73–76	0.90–0.95	33–34	79–85
		STIC1.1	35–41	0.21–0.25	97–100	36–57	35–41	0.93–0.97	15–19	19–25
	AU-Rig	STIC1.0	89–91	0.30–0.33	89–100	22–29	89–91	0.78–0.81	46–60	76–77
		STIC1.1	61–63	0.35–0.43	59–79	59–65	61–63	0.85–0.86	30–45	23–37
	AU-Stp	STIC1.0	70–85	0.65–0.69	82–85	36–50	70–85	0.86–0.89	38–41	86–87
		STIC1.1	46–53	0.75–0.78	52–56	54–60	46–53	0.86–0.87	24–26	6–13
	AU-Whr	STIC1.0	66–84	0.49–0.54	73–88	14–22	66–84	0.90–0.91	30–35	72–80
		STIC1.1	43–44	0.56–0.58	52–53	30–50	43–44	0.93–0.94	21–22	15–21
	AU-Wom	STIC1.0	59–72	0.83–0.84	31–45	9–39	59–72	0.90–0.93	30–32	56–81
		STIC1.1	43–73	0.78–0.84	28–40	39–67	43–73	0.89–0.94	20–38	16–35
Mesic (0.5 < AI)	AU-Cow	STIC1.0	44–59	0.84–0.90	28–37	3–13	44–59	0.77–0.78	44–52	56–78
		STIC1.1	43–47	0.86–0.92	28–29	12–49	43–47	0.81–0.82	43–53	14–20
	AU-Cum	STIC1.0	87–135	0.71–0.78	60–63	28–54	87–135	0.85–0.86	46–53	86–94
		STIC1.1	49–71	0.76–0.84	34–37	5–26	49–71	0.90–0.91	25–33	40–62
	AU-Dry	STIC1.0	93–101	0.70–0.73	57–61	28–29	93–101	0.80–0.81	46–47	83–87
		STIC1.1	65–69	0.77–0.81	41–42	48–59	65–69	0.81–0.82	33–34	9–11
	AU-How	STIC1.0	77–80	0.84–0.85	29–30	13–20	77–80	0.77–0.78	45–50	83–87
		STIC1.1	60–72	0.86–0.88	26–33	27–54	60–72	0.78–0.80	40–49	9–19
	AU-Tum	STIC1.0	63–64	0.86–0.87	28–29	4–8	63–64	0.85–0.86	37–38	52–56
		STIC1.1	58–62	0.85–0.86	26–27	10–14	58–62	0.84–0.86	35–37	13–15

**Table A3**  
*Dry and Wet Seasons of the 15 OzFlux EC Sites Used in the Present Study*

Aridity class	Site name	Season (months)
Arid ( $0 < AI < 0.2$ )	AU-ASM	Wet Jan to Apr
	AU-GWW	Wet Jan to May
	AU-TTE	Wet Jan to Feb
	AU-Cpr	Dry Jan to Mar
	AU-Stp	Wet Jan to Mar
	AU-Gin	Dry Jan to Apr
	AU-Ync	Dry Jan to Mar
	AU-Rig	Dry Jan to Mar
	AU-Whr	Dry Jan to May
	AU-Wom	Dry Jan to Apr
Semi-arid ( $0.2 < AI < 0.5$ )	AU-Cow	Wet Jan to May
	AU-Cum	Wet Jan to Apr
	AU-Dry	Wet Jan to Mar
	AU-How	Wet Jan to Mar
	AU-Tum	Wet Jan to Mar
	AU-Gin	Dry Jan to Oct
	AU-Ync	Dry Jan to Sept
	AU-Rig	Dry Jan to Sept
	AU-Whr	Dry Jun to Sept
	AU-Wom	Dry May to Oct
Mesic ( $0.5 < AI$ )	AU-Cow	Wet Jan to May
	AU-Cum	Wet Jan to Apr
	AU-Dry	Wet Jan to Mar
	AU-How	Wet Jan to Mar
	AU-Tum	Wet Jan to Mar
	AU-Gin	Dry Jan to Oct
	AU-Ync	Dry Jan to Sept
	AU-Rig	Dry Jan to Sept
	AU-Whr	Dry Jun to Sept
	AU-Wom	Dry May to Oct

normalized RMSD (RMSD/standard deviation) and correlation between observed and modeled  $H$  of 27–60% and 0.78–0.95, respectively. Notable differences in  $\lambda E$  errors between wet and dry seasons for arid and semi-arid ecosystems (normalized RMSD 90–100%) were not found, but the error in  $\lambda E$  was lower (52%) during the wet season as compared to the dry seasons (75%) in the mesic ecosystems. This further highlights the fact that the high errors in  $\lambda E$  for dry seasons in arid semi-arid ecosystems are associated with uncertainties in  $T_R$  and SEB closure corrections, respectively.

### A3. Statistical Analysis

Total RMSD is the sum of RMSDs and nonsystematic RMSD (RMSD<sub>U</sub>), and according to Willmott (1982) RMSDs should be less than RMSD<sub>U</sub>. The proportion of the total RMSD arising from systematic biases is reflected in the quantity RMSDs<sup>2</sup>/RMSD<sup>2</sup> (Willmott, 1982).

$$\text{RMSD} = \left[ \frac{1}{N} \sum_{i=1}^N (P_i - O_i)^2 \right]^{0.5} \quad (\text{A1})$$

$$\text{RRMSD} = 100 \left[ \frac{\text{RMSD}}{\bar{O}} \right] \quad (\text{A2})$$

$$\text{MAPD} = \frac{100}{\bar{O}} \left[ \frac{1}{N} \sum_{i=1}^N |(P_i - O_i)| \right] \quad (\text{A3})$$

$$\frac{\text{RMSDs}^2}{\text{RMSD}^2} = 100 \frac{\left[ \frac{1}{N} \sum_{i=1}^N (\hat{P}_i - O_i)^2 \right]^{0.5}}{\left[ \frac{1}{N} \sum_{i=1}^N (P_i - O_i)^2 \right]^{0.5}} \quad (\text{A4})$$

where  $O_i$  represents observed value,  $P_i$  is the model-predicted value,  $N$  number of observations,  $\hat{P}_i$  estimated value based on the ordinary least square regression ( $\hat{P}_i = c + mO_i$ ); where  $m$  and  $c$  are the slope and intercept of linear regression between  $P$  on  $O$ , and  $\bar{O}$  is the mean of observed values.

### Acknowledgments

This study was funded by the Luxembourg Institute of Science and Technology (LIST) under project BIOTRANS (project code 00001145). Partial funding for this research was provided through the FNR-DFG CAOS-2 project grant (INTER/DFG/14/02); and through HiWET (High-resolution modeling and monitoring of Water and Energy Transfers in wetland ecosystems) consortium funded by BELSPO and FNR under the programme STEREOIII (INTER/STEREOIII/13/03/HiWET; contract NR SR/00/301). We are grateful to all Australian and international collaborators, OzFlux PIs, and all the funding agencies that have contributed to establishing Terrestrial Ecosystem Research Network (TERN) and Ozflux. The authors declare no conflict of interest. This work utilized data collected by grants funded by the Australian Research Council (DP0344744, DP0772981, DP120101735, DP130101566, and LE0882936). Jason Beringer is funded under an ARC Future Fellowship (FT110100602). DTD acknowledges support of the Jet Propulsion Laboratory, California Institute of Technology, under a contract with the National Aeronautics and Space Administration. KM designed the analysis; ET and KM performed the analysis; KM, ET, and IT developed the initial version of the manuscript; and all the coauthors make significant contribution in editing the manuscript. The authors declare no conflict of interests. Data used in the current analysis is available through the OzFlux data portal (<http://data.ozflux.org.au/portal/pub/listPubCollections.jspx>), and we have used data level-3 data that was available in csv format in the fluxnet repository (<http://data.ozflux.org.au/portal/pub/viewColDetails.jspx?collection.id=1882723&collection.owner.id=450&viewType=anonymous>).

### References

- Abdi, A. M., Boke-Olén, N., Tenenbaum, D. E., Tagesson, T., Cappaere, B., & Ardö, J. (2017). Evaluating water controls on vegetation growth in the semi-arid Sahel using field and Earth observation data. *Remote Sensing*, 9, 294. <https://doi.org/10.3390/rs9030294>
- Allen, R. G., Pereira, L. S., Raes, D., & Smith, M. (1998). *Crop evapotranspiration: Guidelines for computing crop water requirements* (Irrig. and Drainage Pap. 56). Rome, Italy: Food and Agriculture Organization of the United Nations.
- Anderson, M. C., Allen, R., Morse, A., & Kustas, W. P. (2012). Use of Landsat thermal imagery in monitoring evapotranspiration and managing water resources. *Remote Sensing Environment*, 122, 50–65. <https://doi.org/10.1016/j.rse.2011.08.025>
- Anderson, M. C., Norman, J. M., Kustas, W. P., Houborg, R., Starks, P., & Agam, N. (2008). A thermal-based remote sensing technique for routine mapping of land-surface carbon, water and energy fluxes from field to regional scales. *Remote Sensing of Environment*, 112(12), 4227–4241. <https://doi.org/10.1016/j.rse.2008.07.009>
- Anderson, M. C., Norman, J. M., Mecikalski, J. R., Otkin, J. A., & Kustas, W. P. (2007). A climatological study of evapotranspiration and moisture stress across the continental United States based on thermal remote sensing. 1: Model formulation. *Journal of Geophysical Research*, 112, D10117. <https://doi.org/10.1029/2006JD007506>
- Barr, A. G., van der Kamp, G., Black, T. A., McCaughey, H., & Nesic, Z. (2012). Energy balance closure at the BERMS flux towers in relation to the water balance of the White Gull Creek watershed 1999–2009. *Agricultural and Forest Meteorology*, 153, 3–13. <https://doi.org/10.1016/j.agrformet.2011.05.017>
- Beringer, J., Hutley, L. B., McHugh, I., Arndt, S. K., Campbell, D., Cleugh, H. A., et al. (2016). An introduction to the Australian and New Zealand flux tower network—OzFlux. *Biogeosciences*, 13, 5895–5916. <https://doi.org/10.5194/bg-13-5895-2016>
- Bhattarai, N., Mallick, K., Brunsell, N. A., Sun, G., & Jain, M. (2017). Regional evapotranspiration from image-based implementation of the Surface Temperature Initiated Closure (STIC1.2) model and its validation across an aridity gradient in the conterminous United States. *Hydrology and Earth System Sciences*, 22, 2311–2341. <https://doi.org/10.5194/hess-22-2311-2018>
- Boegh, E., & Soegaard, H. (2004). Remote sensing based estimation of evapotranspiration rates. *International Journal of Remote Sensing*, 25, 2535–2551.
- Boegh, E., Soegaard, H., & Thomsen, A. (2002). Evaluating evapotranspiration rates and surface conditions using Landsat TM to estimate atmospheric resistance and surface resistance. *Remote Sensing Environment*, 79, 329–343.
- Boulet, G., Mougenot, B., Lhomme, J.-P., Fanise, P., Lili-Chabaane, Z., Olioso, A., et al. (2015). The SPARSE model for the prediction of water stress and evapotranspiration components from thermal infra-red data and its evaluation over irrigated and rainfed wheat. *Hydrology and Earth System Sciences*, 19, 4653–4672. <https://doi.org/10.5194/hess-19-4653-2015>
- Boulet, G., Olioso, A., Ceschia, F., Marloie, O., Coudert, B., & Rivalland, A. (2012). An empirical expression to relate aerodynamic and surface temperatures for use within single-source energy balance models. *Agricultural and Forest Meteorology*, 161, 148–155. doi:10.1016/j.agrformet.2012.03.008
- Bowen, I. (1926). The ratio of heat losses by conduction and by evaporation from any water surface. *Physical Review*, 27(6), 779–787. <https://doi.org/10.1103/PhysRev.27.779>
- Brutsaert, W., & Stricker, H. (1979). An advection-aridity approach to estimate actual regional evapotranspiration. *Water Resources Research*, 15(2), 443–450. <https://doi.org/10.1029/WR015i002p00443>
- Chávez, J. L., Howell, T. A., Gowda, P. H., Copeland, K. S., & Prueger, J. H. (2010). Surface aerodynamic temperature modeling over rainfed cotton. *Transactions of the ASABE*, 53(3), 759–767.
- Chávez, J. L., Neale, C. M. U., Hippis, L. E., Prueger, J. H., & Kustas, W. P. (2005). Comparing aircraft-based remotely sensed energy balance fluxes with eddy covariance tower data using heat flux source area functions. *Journal of Hydrometeorology*, 6, 923–940.
- Cleverly, J., Chen, C., Boulain, N., Villalobos-Vega, R., Faux, R., Grant, N., et al. (2013). Aerodynamic resistance and Penman-Monteith evapotranspiration over a seasonally two-layered canopy in semi-arid central Australia. *Journal of Hydrometeorology*, 14, 1562–1570. <https://doi.org/10.1175/jhm-d-13-080.1>
- Cleverly, J., Eamus, D., Van Gorsel, E., Chen, C., Rumman, R., Luod, Q., et al. (2016). Productivity and evapotranspiration of two contrasting semi-arid ecosystems following the 2011 global carbon land sink anomaly. *Agricultural and Forest Meteorology*, 220, 151–159. <https://doi.org/10.1016/j.agrformet.2016.01.086>
- Colaizzi, P. D., Agam, N., Tolk, J. A., Evett, S. R., Howell, T. A., Gowda, P. H., et al. (2014). Two-source energy balance model to calculate E, T, and ET: Comparison of Priestley-Taylor and Penman-Monteith formulations and two time scaling methods. *Transactions of the ASABE*, 57 (2), 479–498. <https://doi.org/10.13031/trans.57.10423>
- Colaizzi, P. D., Evett, S. R., Howell, T. A., & Tolk, J. A. (2004). Comparison of aerodynamic and radiometric surface temperature using precision weighing lysimeters, Remote Sensing and modeling of ecosystems for sustainability. In *Proceedings of SPIE* (Vol. 5544). Bellingham, WA: SPIE. <https://doi.org/10.1117/12.559503>
- Colaizzi, P. D., Kustas, W. P., Anderson, M. C., Agam, N., Tolk, J. A., Evett, S. R., et al. (2012). Two-source energy balance model estimates of evapotranspiration using component and composite surface temperatures. *Advances in Water Research*, 50, 134–151. <https://doi.org/10.1016/j.advwatres.2012.06.004>
- Crado, R. D., & Qualls, R. J. (2014). Use of land surface temperature to estimate surface energy fluxes: Contributions of Wilfried Brutsaert and collaborators. *Water Resources Research*, 50, 3396–3408. <https://doi.org/10.1002/2013WR015223>
- Dirmeyer, P. A. (2011). The terrestrial segment of soil moisture-climate coupling. *Geophysical Research Letters*, 38, L16702. <https://doi.org/10.1029/2011GL048268>
- Donohue, R. J., Roderick, M. L., & McVicar, T. R. (2010). Can dynamic vegetation information improve the accuracy of Budyko's hydrological model? *Journal of Hydrology*, 390, 23–34. <https://doi.org/10.1016/j.jhydrol.2010.06.025>
- Ershadi, A., McCabe, M. F., Evans, J. P., & Wood, E. F. (2015). Impact of model structure and parameterization on Penman-Monteith type evaporation models. *Journal of Hydrology*, 525, 521–535. <https://doi.org/10.1016/j.jhydrol.2015.04.008>
- Foken, T. (2008). The energy balance closure problem: An overview. *Ecological Applications*, 18, 1351–1367. <https://doi.org/10.1890/06-0922.1>
- Formetta, G., Bancheri, M., David, O., & Rigon, R. (2016). Performance of site-specific parameterizations of longwave radiation. *Hydrology and Earth System Sciences*, 20, 4641–4654. <https://doi.org/10.5194/hess-20-4641-2016>.

- French, A. N., Hunsaker, D. J., & Thorp, K. R. (2015). Remote sensing of evapotranspiration over cotton using the TSEB and METRIC energy balance models. *Remote Sensing Environment*, 158, 281–294. <https://doi.org/10.1016/j.rse.2014.11.003>
- García, M., Oyonarte, C., Villagarcía, L., Contreras, S., Domingo, F., & Puigdefábregas, J. (2008). Monitoring land degradation risk using ASTER data: The non-evaporative fraction as an indicator of ecosystem function. *Remote Sensing Environment*, 112, 3720–3736. <https://doi.org/10.1016/j.rse.2008.05.011>
- Glenn, E., Doody, T. M., Guerszman, J. P., Huete, A. R., King, E. A., McVicar, T. R., et al. (2011). Actual evapotranspiration estimation by ground and remote sensing methods: The Australian experience. *Hydrological Processes*, 25, 4103–4116. <https://doi.org/10.1002/hyp.8391>
- Göttsche, F. M., & Hulley, G. C. (2012). Validation of six satellite-retrieved land surface emissivity products over two land cover types in a hyper-arid region. *Remote Sensing Environment*, 124, 149–158.
- Guerszman, J., Van Dijk, A. I. J. M., Mattersdorf, G., Beringer, J., Hutley, L. B., Leuning, R., et al. (2009). Scaling of potential evapotranspiration with MODIS data reproduces flux observations and catchment water balance observations across Australia. *Journal of Hydrology*, 369, 107–119. <https://doi.org/10.1016/j.jhydrol.2009.02.013>
- Heitman, J. L., Horton, R., Sauer, T. J., Ren, T. S., & Xiao, X. (2010). Latent heat in soil heat flux measurements. *Agricultural and Forest Meteorology*, 150, 1147–1153. <https://doi.org/10.1016/j.agrformet.2010.04.017>
- Hollinger, D. Y., & Richardson, A. (2005). Uncertainty in eddy covariance measurements and its application to physiological models. *Tree Physiology*, 25, 783–885. <https://doi.org/10.1093/treephys/25.7.873>
- Holwerda, F., Bruijnzeela, L. A., Scatenac, F. N., Vugtsa, H. F., & Meestersa, A. G. C. A. (2012). Wet canopy evaporation from a Puerto Rican lower montane rain forest: The importance of realistically estimated aerodynamic conductance. *Journal of Hydrology*, 414–415, 1–15. <https://doi.org/10.1016/j.jhydrol.2011.07.033>
- Hulley, G. C., Hook, S. J., Abbott, E., Malakar, N., Islam, T., & Abrams, M. (2015). The ASTER global emissivity dataset (ASTER GED): Mapping Earth's emissivity at 100 meter spatial scale. *Geophysical Research Letters*, 42, 7966–7976. <https://doi.org/10.1002/2015GL065564>
- Hulley, G. C., Hook, S. J., & Baldridge, A. M. (2010). Investigating the effects of soil moisture on thermal infrared land surface temperature and emissivity using satellite retrievals and laboratory measurements. *Remote Sensing Environment*, 114, 1480–1493. <https://doi.org/10.1016/j.rse.2010.02.002>
- Hulley, G. C., Hughes, T., & Hook, S. J. (2012). Quantifying uncertainties in land surface temperature (LST) and emissivity retrievals from ASTER and MODIS thermal infrared data. *Journal of Geophysical Research*, 117, D23113. <https://doi.org/10.1029/2012JD018506>
- Jackson, R. D., Idso, S. B., Regnitz, R. J., & Pinter, P. J. (1981). Canopy temperature as a crop water stress indicator. *Water Resources Research*, 17, 1133–1138. <https://doi.org/10.1029/WR017i004p01133>
- Jarvis, P. G., & McNaughton, K. G. (1986). Stomatal control of transpiration: Scaling up from leaf to region. *Advances in Ecological Research*, 15, 1–49. [https://doi.org/10.1016/S0065-2504\(08\)60119-1](https://doi.org/10.1016/S0065-2504(08)60119-1)
- Jolliffe, I. T. (2002). *Principal component analysis, Series: Springer series in statistics* (2nd ed., Vol. XXIX, 487 p., 28 illus). New York, NY: Springer. ISBN: 978-0-387-95442-4.
- Katul, G., Goltz, S., Hsieh, C. I., Cheng, Y., Mowry, F., & Sigmon, J. (1995). Estimation of surface heat and momentum fluxes using the flux-variance method above uniform and non-uniform terrain. *Boundary-Layer Meteorol*, 74, 237–260. <https://doi.org/10.1007/BF00712120>
- Koster, R. D., Salvucci, G. D., Rigden, A. J., Jung, M., Collatz, G. J., & Schubert, S. D. (2015). The pattern across the continental United States of evapotranspiration variability associated with water availability. *Frontiers in Earth Science*, 3, 35. <https://doi.org/10.3389/feart.2015.00035>
- Kustas, W. P., & Anderson, M. C. (2009). Advances in thermal infrared remote sensing for land surface modeling. *Agricultural and Forest Meteorology*, 149, 2071–2081. <https://doi.org/10.1016/j.agrformet.2009.05.016>
- Kustas, W. P., Nieto, H., Morillas, L., Anderson, M. C., Alfieri, J. G., Hippis, L. E., et al. (2016). Revisiting the paper "Using radiometric surface temperature for surface energy flux estimation in Mediterranean drylands from a two-source perspective. *Remote Sensing Environment*, 184, 645–653. <https://doi.org/10.1016/j.rse.2016.07.024>
- Leuning, R., Zhang, Y., Rajaud, A., Cleugh, H., & Tu, K. (2008). A simple surface conductance model to estimate regional evaporation using MODIS leaf area index and the Penman-Monteith equation. *Water Resources Research*, 44, W10419. <https://doi.org/10.1029/2007WR006562>
- Li, J., Li, J., Weisz, E., & Zhou, D. K. (2007). Physical retrieval of surface emissivity spectrum from hyperspectral infrared radiances. *Geophysical Research Letters*, 34, L16812. <https://doi.org/10.1029/2007GL030543>
- Liu, S., Lu, L., Mao, D., & Jia, L. (2007). Evaluating parameterizations of aerodynamic resistance to heat transfer using field measurements. *Hydrology and Earth System Sciences*, 11, 769–783. <https://doi.org/10.5194/hess-11-769-2007>
- Ma, X., Huete, A., Cleverly, J., Eamus, D., Chevallier, F., Joiner, J., et al. (2016). Drought rapidly diminishes the large net CO<sub>2</sub> uptake in 2011 over semi-arid Australia. *Scientific Reports*, 6, 37747. <https://doi.org/10.1038/srep37747>
- Majoz, N. P., Mannaerts, C. M., Ramoelo, A., Mathieu, R., Nickless, A., & Verhoef, W. (2017). Analysing surface energy balance closure and partitioning over a semi-arid savanna FLUXNET site in Skukuza, Kruger National Park, South Africa. *Hydrology and Earth System Sciences*, 21, 3401–3415. <https://doi.org/10.5194/hess-21-3401-2017>
- Mallick, K., Boegh, E., Trebs, I., Alfieri, J. G., Kustas, W. P., Prueger, J. H., et al. (2015). Reintroducing radiometric surface temperature into the Penman-Monteith formulation. *Water Resources Research*, 51, 6214–6243. <https://doi.org/10.1002/2014WR016106>
- Mallick, K., Jarvis, A. J., Boegh, E., Fisher, J. B., Drewry, D. T., Tu, K. P., et al. (2014a). A surface temperature initiated closure (STIC) for surface energy balance fluxes. *Remote Sensing Environment*, 141, 243–261. <https://doi.org/10.1016/j.rse.2013.10.022>
- Mallick, K., Jarvis, A. J., Wohlfahrt, G., Kiely, G., Hirano, T., Miyata, A., et al. (2014b). Components of near-surface energy balance derived from satellite soundings—Part 2: Noontime latent heat flux. *Biogeosciences*, 11, 7369–7382. <https://doi.org/10.5194/bg-11-7369-2014>
- Mallick, K., Trebs, I., Boegh, E., Giustarini, L., Schlerf, M., Drewry, D. T., et al. (2016). Canopy-scale biophysical controls of transpiration and evaporation in the Amazon Basin. *Hydrology and Earth System Sciences*, 20, 4237–4264. <https://doi.org/10.5194/hess-20-4237-2016>
- Martens, B., Miralles, D., Lievens, H., Fernandez-Prieto, D., & Verhoest, N. (2016). Improving terrestrial evaporation estimates over continental Australia through assimilation of SMOS soil moisture. *International Journal of Applied Earth Observation and Geoinformation*, 48, 146–162. <https://doi.org/10.1016/j.jag.2015.09.012>
- Masiello, G., Serio, C., Venafra, S., DeFeis, I., & Borbas, E. E. (2014). Diurnal variation in Sahara desert sand emissivity during the dry season from IASI observations. *Journal of Geophysical Research: Atmospheres*, 119, 1626–1638. <https://doi.org/10.1002/jgrd.50863>
- Masseroni, D., Corbari, C., & Mancini, M. (2014). Limitations and improvements of the energy balance closure with reference to experimental data measured over a maize field. *Atmosfera*, 27, 335–352. [https://doi.org/10.1016/S0187-6236\(14\)70033-5](https://doi.org/10.1016/S0187-6236(14)70033-5)
- McHugh, T. A., Morrissey, E. M., Reed, S. C., Hungate, B. A., & Schwartz, E. (2015). Water from air: An overlooked source of moisture in arid and semi-arid regions. *Scientific Report*, 5, 13767. <https://doi.org/10.1038/srep13767>
- Mira, M., Valor, E., Boluda, R., Caselles, V., & Coll, C. (2007). Influence of soil water content on the thermal infrared emissivity of bare soils: Implication for land surface temperature determination. *Journal of Geophysical Research*, 112, F04003. <https://doi.org/10.1029/2007JF000749>

- Monteith, J. L. (1965). Evaporation and environment. In G. E. Fogg (Ed.) *Symposium of the society for experimental biology. The state and movement of water in living organisms* (Vol. 19, pp. 205–234). New York, NY: Academic Press, Inc.
- Monteith, J. L. (1981). Evaporation and surface temperature. *Quarterly Journal of the Royal Meteorological Society*, 107, 1–27. <https://doi.org/10.1002/qj.49710745102>
- Monteith, J. L. (1995). Accommodation between transpiring vegetation and the convective boundary layer. *Journal of Hydrology*, 166, 251–263. [https://doi.org/10.1016/0022-1694\(94\)05086-D](https://doi.org/10.1016/0022-1694(94)05086-D)
- Morillas, L., García, M., Nieto, H., Villagarcía, L., Sandholz, I., Gonzalez-Dugo, M., et al. (2013). Using radiometric surface temperature for energy flux estimation in Mediterranean drylands from a two-source perspective. *Remote Sensing Environment*, 136, 234–246. <https://doi.org/10.1016/j.rse.2013.05.010>
- Norman, J. M., Kustas, W. P., & Humes, K. S. (1995). Source approach for estimating soil and vegetation energy fluxes in observations of directional radiometric surface temperature. *Agricultural and Forest Meteorology*, 77, 263–293. [https://doi.org/10.1016/0168-1923\(95\)02265-Y](https://doi.org/10.1016/0168-1923(95)02265-Y)
- Ochsner, T. E., Sauer, T. J., & Horton, R. (2006). Field tests of the soil heat flux plate method and some alternatives. *Agronomy Journal*, 98, 1005–1014. <https://doi.org/10.2134/agronj2005.0249>
- Park, G.-H., Gao, X., & Sorooshian, S. (2008). Estimation of surface longwave radiation components from ground-based historical net radiation and weather data. *Journal of Geophysical Research*, 113, D04207. <https://doi.org/10.1029/2007JD008903>
- Paul, G., Gowda, P., Varaprasad, P., Howell, T. A., Aiken, R., & Neale, C. (2014). Investigating the influence of roughness length for heat transport (zoh) on the performance of SEBAL in semi-arid irrigated and dryland agricultural systems. *Journal of Hydrology*, 509, 231–234. <https://doi.org/10.1016/j.jhydrol.2013.11.040>
- Paul, G., Gowda, P. H., Vara Prasad, P. V., Howell, T. A., & Staggenborg, S. A. (2013). Lysimetric evaluation of SEBAL using high resolution airborne imagery from BEAREX08. *Advances in Water Research*, 59, 157–168. <https://doi.org/10.1016/j.advwatres.2013.06.003>
- Perez, P. J., Castellvi, F., Ibanez, M., & Rosell, J. I. (1999). Assessment of reliability of Bowen ratio method for partitioning fluxes. *Agricultural and Forest Meteorology*, 97, 141–150. [https://doi.org/10.1016/S0168-1923\(99\)00080-5](https://doi.org/10.1016/S0168-1923(99)00080-5)
- Priestley, C. H. B., & Taylor, R. J. (1972). On the assessment of surface heat flux and evaporation using large scale parameters. *Monthly Weather Review*, 100, 81–92. [https://doi.org/10.1175/1520-0493\(1972\)100<081:OTAOSH>2.3.CO;2](https://doi.org/10.1175/1520-0493(1972)100<081:OTAOSH>2.3.CO;2)
- Raupach, M. R. (1998). Influence of local feedbacks on land-air exchanges of energy and carbon. *Global Change Biology*, 4, 477–494. <https://doi.org/10.1046/j.1365-2486.1998.t01-1-00155.x>
- Saadi, S., Boulet, G., Bahir, M., Brut, A., Delogu, É., Fanise, P., et al. (2017). Assessment of actual evapotranspiration over a semi-arid heterogeneous land surface by means of coupled low resolution remote sensing data with energy balance model: Comparison to extra Large Aperture Scintillometer measurements. *Hydrology and Earth System Sciences Discussions*, 22, 2187–2209. <https://doi.org/10.5194/hess-2017-454>
- Shuttleworth, W. J., Gurney, R. J., Hsu, A. Y., & Ormsby, J. P. (1989). FIFE: The variation in energy partition at surface flux sites. In A. Rango (Ed.), *Remote sensing and large scale processes, Proceedings of the IAHS Third International Assembly* (Vol. 186, pp. 67–74). Baltimore, MD, IAHS Publ.
- Shuttleworth, W. J., & Wallace, J. (1985). Evaporation from sparse crops—an energy combination theory. *Quarterly Journal of the Royal Meteorological Society*, 111, 839–855. <https://doi.org/10.1002/qj.49711146910>
- Siqueira, M., Katul, G., & Porporato, A. (2008). Onset of water stress, hysteresis in plant conductance, and hydraulic lift: Scaling soil water dynamics from millimeters to meters. *Water Resources Research*, 44, W01432. <https://doi.org/10.1029/2007WR006094>
- Song, L., Kustas, W. P., Liu, S., Colaizzi, P. D., Nieto, H., Xu, Z., et al. (2016). Applications of a thermal-based two-source energy balance model using Priestley-Taylor approach for surface temperature partitioning under advective conditions. *Journal of Hydrology*, 540, 574–587. <https://doi.org/10.1016/j.jhydrol.2016.06.034>
- Su, Z. (2002). The surface energy balance system (SEBS) for estimation of turbulent heat fluxes. *Hydrology and Earth System Sciences*, 61, 85–99. <https://doi.org/10.5194/hess-6-85-2002>
- Sun, D., & Pinker, R. T. (2003). Estimation of land surface temperature from a Geostationary Operational Environmental Satellite (GOES-8). *Journal of Geophysical Research*, 108 (D11), 4326. <https://doi.org/10.1029/2002JD002422>
- Timmermans, J., Su, Z., van der Tol, C., Verhoef, A., & Verhoef, W. (2013). Quantifying the uncertainty in estimates of surface-atmosphere fluxes through joint evaluation of the SEBS and SCOPE models. *Hydrology and Earth System Sciences*, 17, 1561–1573. <https://doi.org/10.5194/hess-17-1561-2013>
- Troufleau, D., Lhomme, J. P., Monteny, B., & Vidal, A. (1997). Sensible heat flux and radiometric surface temperature over sparse Sahelian vegetation. I: An experimental analysis of kB-1 parameter. *Journal of Hydrology*, 188–189, 815–838. [https://doi.org/10.1016/S0022-1694\(96\)03172-1](https://doi.org/10.1016/S0022-1694(96)03172-1)
- van Dijk, A. I. J. M., Beck, H. E., Crosbie, R. S., de Jeu, R. A. M., Liu, Y. Y., Podger, G. M., et al. (2013). The Millennium Drought in southeast Australia (2001–2009): Natural and human causes and implications for water resources, ecosystems, economy, and society. *Water Resources Research*, 49, 1040–1057. <https://doi.org/10.1020/wrcr.20123>
- van Dijk, A. I. J. M., Gash, J. H., van Gorsel, E., Blanken, P. D., Cescatti, A., Emmel, C., et al. (2015). Rainfall interception and the coupled surface water and energy balance. *Agricultural and Forest Meteorology*, 214–215, 402–415. <https://doi.org/10.1016/j.agrformet.2015.09.006>
- Venturini, V., Islam, S., & Rodriguez, L. (2008). Estimation of evaporative fraction and evapotranspiration from MODIS products using a complementary based model. *Remote Sensing Environment*, 112, 132–141. <https://doi.org/10.1016/j.rse.2007.04.014>
- Wang, J., Zhuang, J., Wang, W., Liu, S., & Xu, Z. (2015). Assessment of uncertainty in eddy covariance flux measurement based on intensive flux matrix of HiWATER-MUSOEXE. *IEEE Geoscience and Remote Sensing Letters*, 12 (2), 259–264. <https://doi.org/10.1109/LGRS.2014.2334703>
- Willmott, C. J. (1982). Some comments on the evaluation of model performance. *Bulletin of the American Meteorological Society*, 63, 1309–1313. [https://doi.org/10.1175/1520-0477\(1982\)063<1309:SCOTEO>2.0.CO;2](https://doi.org/10.1175/1520-0477(1982)063<1309:SCOTEO>2.0.CO;2)
- Winter, J. M., & Eltahir, E. A. B. (2010). The sensitivity of latent heat flux to changes in the radiative forcing: A framework for comparing models and observations. *Journal of Climate*, 23, 2345–2356. <https://doi.org/10.1175/2009JCLI3158.1>
- Zhang, Q., Manzoni, S., Katul, G., Porporato, A., & Yang, D. (2014). The hysteretic evapotranspiration—Vapor pressure deficit relation. *Journal of Geophysical Research: Biogeosciences*, 119, 125–140. <https://doi.org/10.1002/2013JG002484>